

The first year of the *BABAR* experiment at PEP-II

The *BABAR* Collaboration

June 17, 2018

Abstract

The *BABAR* detector, situated at the SLAC PEP-II asymmetric e^+e^- collider, has been recording data at energies on and around the $\Upsilon(4S)$ resonance since May 1999. In this paper, we briefly describe the PEP-II *B* Factory and the *BABAR* detector. The performance presently achieved by the experiment in the areas of tracking, vertexing, calorimetry and particle identification is reviewed. Analysis concepts that are used in the various papers submitted to this conference are also discussed.

The BABAR Collaboration

B. Aubert, A. Boucham, D. Boutigny, I. De Bonis, J. Favier, J.-M. Gaillard, F. Galeazzi, A. Jeremie,
Y. Karyotakis, J. P. Lees, P. Robbe, V. Tisserand, K. Zachariadou

Lab de Phys. des Particules, F-74941 Annecy-le-Vieux, CEDEX, France

A. Palano

Università di Bari, Dipartimento di Fisica and INFN, I-70126 Bari, Italy

G. P. Chen, J. C. Chen, N. D. Qi, G. Rong, P. Wang, Y. S. Zhu

Institute of High Energy Physics, Beijing 100039, China

G. Eigen, P. L. Reinertsen, B. Stugu

University of Bergen, Inst. of Physics, N-5007 Bergen, Norway

B. Abbott, G. S. Abrams, A. W. Borgland, A. B. Breon, D. N. Brown, J. Button-Shafer, R. N. Cahn,
A. R. Clark, Q. Fan, M. S. Gill, S. J. Gowdy, Y. Groysman, R. G. Jacobsen, R. W. Kadel, J. Kadyk,
L. T. Kerth, S. Kluth, J. F. Kral, C. Leclerc, M. E. Levi, T. Liu, G. Lynch, A. B. Meyer, M. Momayezi,
P. J. Oddone, A. Perazzo, M. Pripstein, N. A. Roe, A. Romosan, M. T. Ronan, V. G. Shelkov, P. Strother,
A. V. Telnov, W. A. Wenzel

Lawrence Berkeley National Lab, Berkeley, CA 94720, USA

P. G. Bright-Thomas, T. J. Champion, C. M. Hawkes, A. Kirk, S. W. O'Neale, A. T. Watson, N. K. Watson

University of Birmingham, Birmingham, B15 2TT, UK

T. Deppermann, H. Koch, J. Krug, M. Kunze, B. Lewandowski, K. Peters, H. Schmuecker, M. Steinke

Ruhr Universität Bochum, Inst. f. Experimentalphysik 1, D-44780 Bochum, Germany

J. C. Andress, N. Chevalier, P. J. Clark, N. Cottingham, N. De Groot, N. Dyce, B. Foster, A. Mass,
J. D. McFall, D. Wallom, F. F. Wilson

University of Bristol, Bristol BS8 1TL, UK

K. Abe, C. Hearty, T. S. Mattison, J. A. McKenna, D. Thiessen

University of British Columbia, Vancouver, BC, Canada V6T 1Z1

B. Camanzi, A. K. McKemey, J. Tinslay

Brunel University, Uxbridge, Middlesex UB8 3PH, UK

V. E. Blinov, A. D. Bukin, D. A. Bukin, A. R. Buzykaev, M. S. Dubrovin, V. B. Golubev,
V. N. Ivanchenko, A. A. Korol, E. A. Kravchenko, A. P. Onuchin, A. A. Salmikov, S. I. Serednyakov,
Yu. I. Skovpen, A. N. Yushkov

*Budker Institute of Nuclear Physics, Siberian Branch of Russian Academy of Science, Novosibirsk 630090,
Russia*

A. J. Lankford, M. Mandelkern, D. P. Stoker

University of California at Irvine, Irvine, CA 92697, USA

A. Ahsan, K. Arisaka, C. Buchanan, S. Chun

University of California at Los Angeles, Los Angeles, CA 90024, USA

J. G. Branson, R. Faccini,¹ D. B. MacFarlane, Sh. Rahatlou, G. Raven, V. Sharma
University of California at San Diego, La Jolla, CA 92093, USA

C. Campagnari, B. Dahmes, P. A. Hart, N. Kuznetsova, S. L. Levy, O. Long, A. Lu, J. D. Richman,
W. Verkerke, M. Witherell, S. Yellin
University of California at Santa Barbara, Santa Barbara, CA 93106, USA

J. Beringer, D. E. Dorfan, A. Eisner, A. Frey, A. A. Grillo, M. Grothe, C. A. Heusch, R. P. Johnson,
W. Kroeger, W. S. Lockman, T. Pulliam, H. Sadrozinski, T. Schalk, R. E. Schmitz, B. A. Schumm,
A. Seiden, M. Turri, D. C. Williams
University of California at Santa Cruz, Institute for Particle Physics, Santa Cruz, CA 95064, USA

E. Chen, G. P. Dubois-Felsmann, A. Dvoretzkii, D. G. Hitlin, Yu. G. Kolomensky, S. Metzler, J. Oyang,
F. C. Porter, A. Ryd, A. Samuel, M. Weaver, S. Yang, R. Y. Zhu
California Institute of Technology, Pasadena, CA 91125, USA

R. Aleksan, G. De Domenico, A. de Lesquen, S. Emery, A. Gaidot, S. F. Ganzhur, G. Hamel de
Monchenault, W. Kozanecki, M. Langer, G. W. London, B. Mayer, B. Serfass, G. Vasseur, C. Yeche,
M. Zito
Centre d'Etudes Nucléaires, Saclay, F-91191 Gif-sur-Yvette, France

S. Devmal, T. L. Geld, S. Jayatilleke, S. M. Jayatilleke, G. Mancinelli, B. T. Meadows, M. D. Sokoloff
University of Cincinnati, Cincinnati, OH 45221, USA

J. Blouw, J. L. Harton, M. Krishnamurthy, A. Soffer, W. H. Toki, R. J. Wilson, J. Zhang
Colorado State University, Fort Collins, CO 80523, USA

S. Fahey, W. T. Ford, F. Gaede, D. R. Johnson, A. K. Michael, U. Nauenberg, A. Olivas, H. Park,
P. Rankin, J. Roy, S. Sen, J. G. Smith, D. L. Wagner
University of Colorado, Boulder, CO 80309, USA

T. Brandt, J. Brose, G. Dahlinger, M. Dickopp, R. S. Dubitzky, M. L. Kocian, R. Müller-Pfefferkorn,
K. R. Schubert, R. Schwierz, B. Spaan, L. Wilden
Technische Universität Dresden, Inst. f. Kern- u. Teilchenphysik, D-01062 Dresden, Germany

L. Behr, D. Bernard, G. R. Bonneaud, F. Brochard, J. Cohen-Tanugi, S. Ferrag, E. Roussot, C. Thiebaut,
G. Vasileiadis, M. Verderi
Ecole Polytechnique, Lab de Physique Nucléaire H. E., F-91128 Palaiseau, France

A. Anjomshoaa, R. Bernet, F. Di Lodovico, F. Muheim, S. Playfer, J. E. Swain
University of Edinburgh, Edinburgh EH9 3JZ, UK

C. Bozzi, S. Dittongo, M. Folegani, L. Piemontese
Università di Ferrara, Dipartimento di Fisica and INFN, I-44100 Ferrara, Italy

E. Treadwell
Florida A&M University, Tallahassee, FL 32307, USA

¹ Jointly appointed with Università di Roma La Sapienza, Dipartimento di Fisica and INFN, I-00185 Roma, Italy

R. Baldini-Ferroli, A. Calcaterra, R. de Sangro, D. Falciari, G. Finocchiaro, P. Patteri, I. M. Peruzzi,²
M. Piccolo, A. Zallo

Laboratori Nazionali di Frascati dell'INFN, I-00044 Frascati, Italy

S. Bagnasco, A. Buzzo, R. Contri, G. Crosetti, P. Fabbriatore, S. Farinon, M. Lo Vetere, M. Macri,
M. R. Monge, R. Musenich, R. Parodi, S. Passaggio, F. C. Pastore, C. Patrignani, M. G. Pia, C. Priano,
E. Robutti, A. Santroni

Università di Genova, Dipartimento di Fisica and INFN, I-16146 Genova, Italy

J. Cochran, H. B. Crawley, P.-A. Fischer, J. Lamsa, W. T. Meyer, E. I. Rosenberg
Iowa State University, Ames, IA 50011-3160, USA

R. Bartoldus, T. Dignan, R. Hamilton, U. Mallik
University of Iowa, Iowa City, IA 52242, USA

C. Angelini, G. Batignani, S. Bettarini, M. Bondioli, M. Carpinelli, F. Forti, M. A. Giorgi, A. Lusiani,
M. Morganti, E. Paoloni, M. Rama, G. Rizzo, F. Sandrelli, G. Simi, G. Triggiani

Università di Pisa, Scuola Normale Superiore, and INFN, I-56010 Pisa, Italy

M. Benkebil, G. Grosdidier, C. Hast, A. Hoecker, V. LePeltier, A. M. Lutz, S. Plaszczynski, M. H. Schune,
S. Trincaz-Duvoid, A. Valassi, G. Wormser

LAL, F-91898 ORSAY Cedex, France

R. M. Bionta, V. Brigljević, O. Fackler, D. Fujino, D. J. Lange, M. Mugge, X. Shi, T. J. Wenaus,
D. M. Wright, C. R. Wuest

Lawrence Livermore National Laboratory, Livermore, CA 94550, USA

M. Carroll, J. R. Fry, E. Gabathuler, R. Gamet, M. George, M. Kay, S. McMahon, T. R. McMahon,
D. J. Payne, C. Touramanis

University of Liverpool, Liverpool L69 3BX, UK

M. L. Aspinwall, P. D. Dauncey, I. Eschrich, N. J. W. Gunawardane, R. Martin, J. A. Nash, P. Sanders,
D. Smith

University of London, Imperial College, London, SW7 2BW, UK

D. E. Azzopardi, J. J. Back, P. Dixon, P. F. Harrison, P. B. Vidal, M. I. Williams

University of London, Queen Mary and Westfield College, London, E1 4NS, UK

G. Cowan, M. G. Green, A. Kurup, P. McGrath, I. Scott

University of London, Royal Holloway and Bedford New College, Egham, Surrey TW20 0EX, UK

D. Brown, C. L. Davis, Y. Li, J. Pavlovich, A. Trunov

University of Louisville, Louisville, KY 40292, USA

J. Allison, R. J. Barlow, J. T. Boyd, J. Fullwood, A. Khan, G. D. Lafferty, N. Savvas, E. T. Simopoulos,
R. J. Thompson, J. H. Weatherall

University of Manchester, Manchester M13 9PL, UK

² Jointly appointed with Univ. di Perugia, I-06100 Perugia, Italy

C. Dallapiccola, A. Farbin, A. Jawahery, V. Lillard, J. Olsen, D. A. Roberts
University of Maryland, College Park, MD 20742, USA

B. Brau, R. Cowan, F. Taylor, R. K. Yamamoto
Massachusetts Institute of Technology, Lab for Nuclear Science, Cambridge, MA 02139, USA

G. Blaylock, K. T. Flood, S. S. Hertzbach, R. Kofler, C. S. Lin, S. Willocq, J. Wittlin
University of Massachusetts, Amherst, MA 01003, USA

P. Bloom, D. I. Britton, M. Milek, P. M. Patel, J. Trischuk
McGill University, Montreal, PQ, Canada H3A 2T8

F. Lanni, F. Palombo
Università di Milano, Dipartimento di Fisica and INFN, I-20133 Milano, Italy

J. M. Bauer, M. Booke, L. Cremaldi, R. Kroeger, J. Reidy, D. Sanders, D. J. Summers
University of Mississippi, University, MS 38677, USA

J. F. Arguin, J. P. Martin, J. Y. Nief, R. Seitz, P. Taras, A. Woch, V. Zacek
Université de Montreal, Lab. Rene J. A. Levesque, Montreal, QC, Canada, H3C 3J7

H. Nicholson, C. S. Sutton
Mount Holyoke College, South Hadley, MA 01075, USA

N. Cavallo, G. De Nardo, F. Fabozzi, C. Gatto, L. Lista, D. Piccolo, C. Sciacca
Università di Napoli Federico II, Dipartimento di Scienze Fisiche and INFN, I-80126 Napoli, Italy

M. Falbo
Northern Kentucky University, Highland Heights, KY 41076, USA

J. M. LoSecco
University of Notre Dame, Notre Dame, IN 46556, USA

J. R. G. Alsmiller, T. A. Gabriel, T. Handler
Oak Ridge National Laboratory, Oak Ridge, TN 37831, USA

F. Colecchia, F. Dal Corso, G. Michelon, M. Morandin, M. Posocco, R. Stroili, E. Torassa, C. Voci
Università di Padova, Dipartimento di Fisica and INFN, I-35131 Padova, Italy

M. Benayoun, H. Briand, J. Chauveau, P. David, C. De la Vaissière, L. Del Buono, O. Hamon, F. Le Diberder, Ph. Leruste, J. Lory, F. Martinez-Vidal, L. Roos, J. Stark, S. Versillé
Universités Paris VI et VII, Lab de Physique Nucléaire H. E., F-75252 Paris, Cedex 05, France

P. F. Manfredi, V. Re, V. Speziali
Università di Pavia, Dipartimento di Elettronica and INFN, I-27100 Pavia, Italy

E. D. Frank, L. Gladney, Q. H. Guo, J. H. Panetta
University of Pennsylvania, Philadelphia, PA 19104, USA

M. Haire, D. Judd, K. Paick, L. Turnbull, D. E. Wagoner
Prairie View A&M University, Prairie View, TX 77446, USA

J. Albert, C. Bula, M. H. Kelsey, C. Lu, K. T. McDonald, V. Miftakov, S. F. Schaffner, A. J. S. Smith,
A. Tumanov, E. W. Varnes

Princeton University, Princeton, NJ 08544, USA

G. Cavoto, F. Ferrarotto, F. Ferroni, K. Fratini, E. Lamanna, E. Leonardi, M. A. Mazzoni, S. Morganti,
G. Piredda, F. Safai Tehrani, M. Serra

Università di Roma La Sapienza, Dipartimento di Fisica and INFN, I-00185 Roma, Italy

R. Waldi

Universität Rostock, D-18051 Rostock, Germany

P. F. Jacques, M. Kalelkar, R. J. Plano

Rutgers University, New Brunswick, NJ 08903, USA

T. Adye, U. Egede, B. Franek, N. I. Geddes, G. P. Gopal

Rutherford Appleton Laboratory, Chilton, Didcot, Oxon., OX11 0QX, UK

N. Coptly, M. V. Purohit, F. X. Yumiceva

University of South Carolina, Columbia, SC 29208, USA

I. Adam, P. L. Anthony, F. Anulli, D. Aston, K. Baird, E. Bloom, A. M. Boyarski, F. Bulos, G. Calderini,
M. R. Convery, D. P. Coupal, D. H. Coward, J. Dorfan, M. Doser, W. Dunwoodie, T. Glanzman,
G. L. Godfrey, P. Grosso, J. L. Hewett, T. Himel, M. E. Huffer, W. R. Innes, C. P. Jessop, P. Kim,
U. Langenegger, D. W. G. S. Leith, S. Luitz, V. Luth, H. L. Lynch, G. Manzin, H. Marsiske, S. Menke,
R. Messner, K. C. Moffeit, M. Morii, R. Mount, D. R. Muller, C. P. O'Grady, P. Paolucci, S. Petrak,
H. Quinn, B. N. Ratcliff, S. H. Robertson, L. S. Rochester, A. Roodman, T. Schietinger, R. H. Schindler,
J. Schwiening, G. Sciolla, V. V. Serbo, A. Snyder, A. Soha, S. M. Spanier, A. Stahl, D. Su, M. K. Sullivan,
M. Talby, H. A. Tanaka, J. Va'vra, S. R. Wagner, A. J. R. Weinstein, W. J. Wisniewski, C. C. Young

Stanford Linear Accelerator Center, Stanford, CA 94309, USA

P. R. Burchat, C. H. Cheng, D. Kirkby, T. I. Meyer, C. Roat

Stanford University, Stanford, CA 94305-4060, USA

A. De Silva, R. Henderson

TRIUMF, Vancouver, BC, Canada V6T 2A3

W. Bugg, H. Cohn, E. Hart, A. W. Weidemann

University of Tennessee, Knoxville, TN 37996, USA

T. Benninger, J. M. Izen, I. Kitayama, X. C. Lou, M. Turcotte

University of Texas at Dallas, Richardson, TX 75083, USA

F. Bianchi, M. Bona, B. Di Girolamo, D. Gamba, A. Smol, D. Zanin

Università di Torino, Dipartimento di Fisica Sperimentale and INFN, I-10125 Torino, Italy

L. Bosisio, G. Della Ricca, L. Lanceri, A. Pompili, P. Poropat, M. Prest, E. Vallazza, G. Vuagnin

Università di Trieste, Dipartimento di Fisica and INFN, I-34127 Trieste, Italy

R. S. Panvini

Vanderbilt University, Nashville, TN 37235, USA

C. M. Brown, P. D. Jackson, R. Kowalewski, J. M. Roney
University of Victoria, Victoria, BC, Canada V8W 3P6

H. R. Band, E. Charles, S. Dasu, P. Elmer, J. R. Johnson, J. Nielsen, W. Orejudos, Y. Pan, R. Prepost,
I. J. Scott, J. Walsh, S. L. Wu, Z. Yu, H. Zobernig
University of Wisconsin, Madison, WI 53706, USA

Contents

1	Introduction	10
2	The PEP-II B Factory	10
2.1	Machine Backgrounds	12
3	The <i>BABAR</i> Detector	13
3.1	Silicon Vertex Tracker	14
3.2	Drift Chamber	17
3.3	Particle Identification System	19
3.4	Electromagnetic Calorimeter	20
3.5	Instrumented Flux Return	22
3.6	Trigger	23
3.6.1	Level-1 Trigger	23
3.6.2	Level-3 Trigger	23
3.7	Data Acquisition and Online System	24
3.8	Online Prompt Reconstruction	25
3.9	Computing System	25
4	Data Sample	26
4.1	Delivered and Recorded Integrated Luminosity	26
4.2	Off-Resonance Running	26
4.3	Data Quality	27
5	Simulation	27
5.1	Event Generators	27
5.2	The GEANT3 Model	28
5.3	The Detector Response Simulation	28
6	Tracking and Vertexing	29
6.1	Track Finding and Kalman Filtering	29
6.2	Tracking Efficiency	29
6.3	Slow Pion Reconstruction	30
6.4	Vertex and Kinematic Fitting	31
6.4.1	Beam spot and primary vertex determination	32
6.4.2	Reconstruction of the tagging- B vertex	32
7	Particle Identification	33
7.1	Charged Particle Identification	33
7.1.1	Electrons	33
7.1.2	Muons	33
7.1.3	Charged hadrons	35
7.2	Neutral Particle Identification	35
7.2.1	Photons	35
7.2.2	π^0 and η Reconstruction	37
7.2.3	Neutral Hadrons	38

8	Common Analysis Issues	40
8.1	Centre of Mass Energy and Boost	40
8.2	Continuum Rejection Variables	40
8.3	Event Selection and B Counting	41
8.3.1	Fiducial regions	41
8.3.2	Multi-Hadron selection	41
8.3.3	Muon pair selection	41
8.4	Offline Luminosity Determination	42
8.5	B Counting	42
8.6	Exclusive B Reconstruction Variables	42
8.6.1	Kinematic variables	42
8.6.2	Background parametrisation	43
9	Conclusions and Prospects	44
10	Acknowledgments	44

1 Introduction

The principal goal of an asymmetric B Factory running at energies on and around the $\Upsilon(4S)$ resonance is the comprehensive study of CP violation in B meson systems. The asymmetry in beam energies makes possible the measurement of time-dependent CP violating asymmetries in the decay of neutral B mesons.

CP asymmetries in the B meson system are expected to be large, so that relatively small samples of events are needed to provide accurate measurements. Unfortunately, the B meson decay channels of interest for the study of CP violation have extremely small branching fractions, of order of 10^{-4} or below. In order to measure asymmetries with errors at the 10% level or better, samples of several tens of million neutral B meson pairs are needed. The new generation of B factories must therefore have unprecedented luminosities, in the range 10^{33} to 10^{34} $\text{cm}^{-2}\text{s}^{-1}$.

2 The PEP-II B Factory

The PEP-II B Factory is an e^+e^- colliding beam storage ring complex designed to produce a luminosity of at least 3×10^{33} $\text{cm}^{-2}\text{s}^{-1}$ at $E_{\text{CM}} = 10.58$ GeV, the mass of the $\Upsilon(4S)$ resonance. PEP-II has been constructed by a collaboration of SLAC, LBNL and LLNL [1] on the SLAC site. The machine is asymmetric with energies of 9.0 GeV for the electron beam and 3.1 GeV for the positron beam. The unequal beam energies require a two-ring configuration: electrons in a High Energy Ring (HER) colliding with positrons in the Low Energy Ring (LER). Some accelerator parameters and achievements of the High Energy Ring are listed in Table 1, those of the Low Energy Ring in Table 2. The electrons and positrons are produced by the SLAC Linac, whose high intensity makes it optimal to recharge the beams in “top-off” mode whenever the luminosity drops to about 90% of its peak value.

Table 1: PEP-II High Energy Ring Performance Results.

Parameter	units	Design	Best Achieved	Typical in-run
Energy	GeV	9.0	9.0, ramp to 9.1 & back	9.0, ramp 8.84-9.04
Number of Bunches		1658	1658	553-829
Total Beam Current	A	0.75 (1.0)	0.92	0.70
Beam Lifetime		4hrs @ 1A	11hrs @ 0.9A	9hrs @ 0.70A

Table 2: PEP-II Low Energy Ring Performance Results.

Parameter	units	Design	Best Achieved	Typical in-run
Energy	GeV	3.1	3.1	3.1
Number of Bunches		1658	1658	553-829
Total Beam Current	A	2.14	1.72	1.10
Beam Lifetime		4hrs @ 2A	3.3hrs @ 1.4A	3hrs @ 1.1A

The rings are housed in the 2.2 km former PEP tunnel but with distinct vacuum and accelerating

structures. The High Energy Ring (HER) reuses the magnets of the old PEP machine whereas the Low Energy Ring (LER) is new and is put in place on top of the HER. The PEP-II design has 1658 bunches, each containing 2.1×10^{10} electrons (HER) and 5.9×10^{10} positrons (LER), spaced at 4.2 ns. The RF system provides a total power of 5.1 MW from seven klystron stations driving 24 conventional copper 476 MHz RF cavities. Bunches are brought into a common vacuum chamber and septum at a few nTorr and into head-on collisions in an interaction region within a 2.5 cm-radius beryllium beam-pipe, around which *BABAR* is located.

Asymmetric collisions produce a center of mass energy of 10.58 GeV with a boost of $\beta\gamma = 0.56$ in the lab frame, thereby allowing a measurement of time dependent *CP* violating asymmetries. Such a boost produces an average separation of $\beta\gamma c\tau = 250 \mu\text{m}$ between the two *B* vertices, which is crucial for studying the cleanest and most promising *CP* violating modes.

The PEP-II e^+e^- collider became operational in July 1998 with the completion of the LER. The first collisions were seen shortly thereafter. Fall and winter 1998 PEP-II runs concentrated on raising the beam currents and increasing the luminosity. In February 1999, the peak luminosity reached $5.2 \times 10^{32} \text{ cm}^{-2}\text{s}^{-1}$. In a two month spring down time, the *BABAR* detector was installed. PEP-II turned on May 10th and *BABAR* saw its first hadronic event on May 26th 1999. In August 1999, PEP-II passed the world record for luminosity, achieving $8.1 \times 10^{32} \text{ cm}^{-2}\text{s}^{-1}$. The present luminosity in PEP-II is $2.17 \times 10^{33} \text{ cm}^{-2}\text{s}^{-1}$, or about 72% of the design goal. In June 2000, PEP-II delivered an integrated luminosity of 150 pb^{-1} in one day, above the design goal for daily integrated luminosity of 135 pb^{-1} . Through July 6, PEP-II has delivered over 13.8 fb^{-1} to *BABAR*, of which 12.7 fb^{-1} have been logged by the detector. Beam parameters and luminosity performance results are shown in Table 3. The present plan is to collide until the end of October 2000 followed by a three month installation period. A detailed status report of the current PEP-II performance can be found in Ref. [2].

Table 3: PEP-II Luminosity Performance.

Parameter	units	Design	Best Achieved	Typical in- run
Peak Luminosity	$\text{cm}^{-2}\text{s}^{-1}$	3×10^{33}	2.2×10^{33}	2.0×10^{33}
Specific Luminosity	$\text{cm}^{-2}\text{s}^{-1}/\text{bunch}$	3.1×10^{30}	2.9×10^{30}	1.8×10^{30}
IP Hor. Spot Size Σ_X	μm	220	190	
IP Ver. Spot Size Σ_Y	μm	6.7	6.0	
Top-off Time	minutes	3	2	3
Fill Time	minutes	6	8	10
Integrated Luminosity	$\text{pb}^{-1}/8 \text{ hours}$		54	
	$\text{pb}^{-1}/\text{day}$	135	154	
	$\text{fb}^{-1}/\text{week}$		0.8	
	$\text{fb}^{-1}/\text{month}$		2.7	
Total Integrated Luminosity (thru 7/20/2000)	fb^{-1}		15.4	

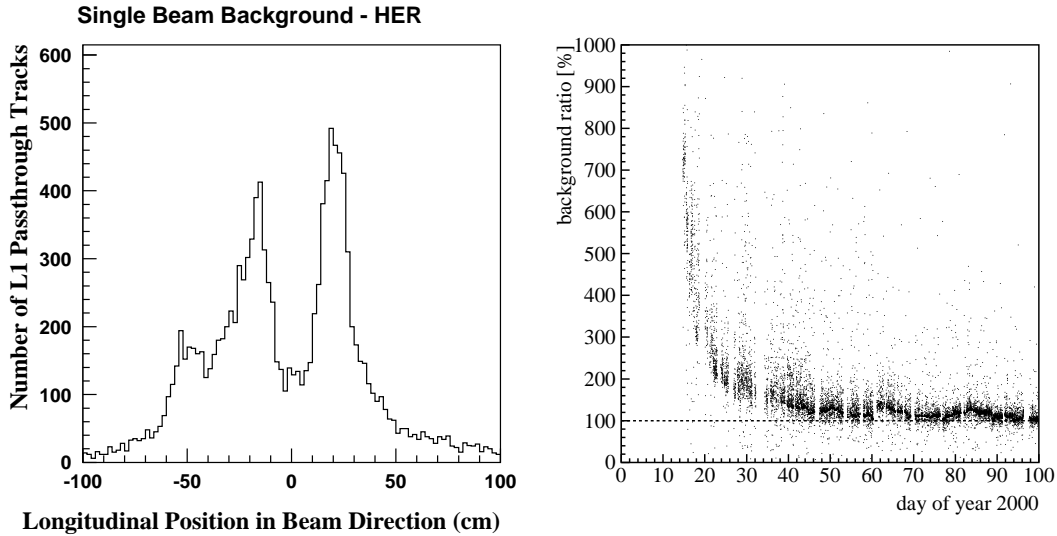


Figure 1: Left: z_0 distribution of L1 pass-through tracks at their point of closest approach to the beam line. Right: Time-history of the DCH current, normalized to that expected, at the same beam currents and luminosity, from background measurements performed in July 2000. The exponential decrease during the first two months of operation reflects the scrubbing, by synchrotron-radiation photons, of residual gas molecules off the vacuum-pipe wall.

2.1 Machine Backgrounds

Operationally, the acceptable level of backgrounds is determined primarily by the radiation hardness of the Silicon Vertex Tracker (SVT) and Electromagnetic Calorimeter (EMC) detectors, and by requiring a tolerable Drift Chamber (DCH) current. The Level-1 (L1) trigger rate and the occupancy in the other detector systems also constitute occasional limitations. Careful measurement, analysis and simulation of the background sources and their impact have led to a detailed understanding and an effective remediation of their effects.

The primary causes of steady-state backgrounds in PEP-II are, in order of increasing importance:

- Synchrotron radiation generated in the bending magnets and final focusing quadrupoles in the incoming HER and LER beam lines. Careful layout of the interaction-region area and a conservative synchrotron radiation masking scheme have proven very effective against these sources.
- The interaction of beam particles with residual gas around the rings (beam-gas), which constitutes the primary source of radiation damage and has had, averaged over this first run, the largest impact on operational efficiency.
- Collision-related electromagnetic shower debris, dominated by energy-degraded e^\pm from radiative-Bhabha scattering which strike vacuum components within a few meters of the interaction point (IP). This background, directly proportional to the instantaneous luminosity, was barely detectable in early running; it now noticeably affects all detectors except the SVT.

While instantaneous background conditions vary because of interaction point orbit drifts and sensitivity of beam tails to small tune adjustments, reproducible patterns have emerged.

The relative importance of the single-beam and luminosity contributions varies from one detector system to the next. The HER beam-gas contribution significantly impacts all detectors except the particle identification system (DIRC): the combination of a 40 m long straight section, almost devoid of magnetic bending upstream of the final doublet, and of the magnetic beam-separation scheme, result in abundant bremsstrahlung-induced electromagnetic debris being directed onto the IP vacuum pipe. The same process occurs in the LER, but to a lesser extent (for a given beam current) because of a shorter drift section and lower primary energy. Most detectors, therefore, exhibit occupancy peaks at $\phi = 0$ and 180° , reflecting the fact that the separation dipoles bend energy-degraded particles in opposite directions. Such local beam-gas interactions contribute noticeably to the DCH current; they dominate the SVT instantaneous dose rate in the horizontal plane, the EMC crystal occupancy above the cluster-seeding threshold (10 MeV), and the L1 trigger rate. Analysis of pass-through events from the charged L1 trigger shows that the beam-pipe wall and several aperture restrictions within 100 cm of the interaction point are the primary impact points for lost particles, as illustrated for the HER in Figure 1 (left)). To minimize this background it is vital to maintain a low pressure in the region from 4 m to 60 m upstream of the interaction point in the incoming HER and LER beam lines. Scrubbing, which has reduced the average dynamic pressure in both rings to levels close to or below the design value, also proved effective (Figure 1 (right)).

Under typical running conditions, the DIRC and the DCH receive comparable contributions from beam-gas Coulomb scatters around the entire LER, and from luminosity backgrounds. In addition, these two detectors proved particularly vulnerable to tails generated by beam-beam or electron-cloud induced blowup of the low-energy beam. Even though partially eliminated by a set of betatron collimators in the last arc, such tails - which are very sensitive to accelerator conditions and tuning procedures - tend to scrape near the highest- β point of the final LER doublet, located inside the DIRC's standoff-box (SOB). The resulting background fluctuations occasionally cause the DCH high-voltage protection system to trip, or the counting rate in the DIRC photomultipliers to exceed 200 kHz. The problem could be only partially alleviated by local lead shielding; additional collimation will be installed during the fall 2000 shutdown.

While trigger-rate and occupancy considerations define acceptable dynamic running conditions, it is the total integrated radiation dose that determines the lifetime of the detector systems. Despite a significant investment in radiation-hard technology, the innermost silicon layers of the SVT and its front-end electronics remain the most susceptible to radiation damage. The accumulated dose has been maintained below budget, as shown in Figure 2, through a strict program of hardware interlocks, administrative controls, and real-time monitoring. As of this conference, the worst irradiated spot of the SVT has been exposed to approximately 300 kRad, 20 to 30% of which is contributed by injection periods.

3 The *BABAR* Detector

The new magnetic spectrometer *BABAR* (Figure 3) has been constructed at SLAC, by a collaboration of nine countries, to precisely measure e^+e^- annihilations at center of mass energy $\sqrt{s} \sim 10$ GeV produced with the new PEP-II Asymmetric Storage Rings. Construction of this detector was approved in November 1995 and its commissioning followed in the Fall of 1998. First data with PEP-II colliding beams was collected in May 1999.

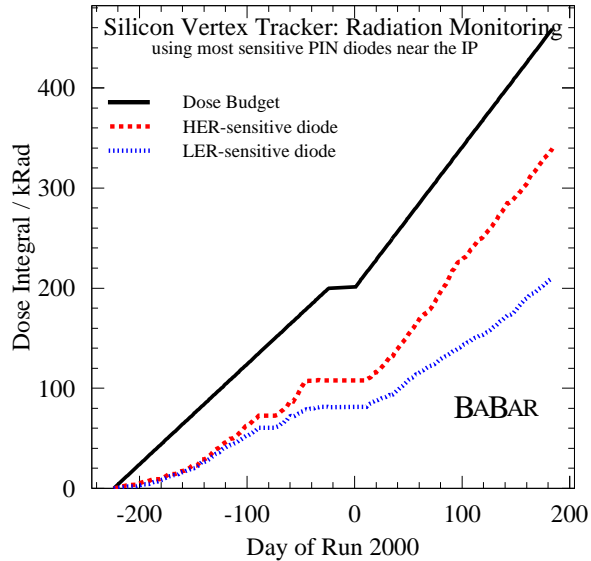


Figure 2: projected History plot of accumulated radiation dose in the SVT using PIN diodes near the interaction point in the horizontal plane (the black line represents the allotted budget, rationing out a 2 MRad dose over the detector’s planned life span).

The *BABAR* superconducting solenoid, which produces a 1.5T axial magnetic field, contains a set of nested detectors: a five-layer silicon-strip vertex detector (SVT), a central Drift Chamber (DCH) for charged particle detection and momentum measurement, a quartz-bar Cherenkov radiation detector (DIRC) for particle identification, and a CsI crystal Electromagnetic Calorimeter (EMC) for detecting photons and separating electrons from charged pions. The calorimeter has a barrel section, and an endcap which extends it asymmetrically into the forward direction (e^- beam direction), where many of the collision products emerge. (There is no calorimeter coverage in the backward direction.) Two layers of cylindrical resistive plate chambers (RPCs) are located between the barrel calorimeter and the magnet cryostat. All the detectors located inside the magnet have full acceptance in azimuth. The Instrumented Flux Return (IFR) outside the cryostat is composed of 18 layers of steel, which increase in thickness outward, and contains 19 layers of planar RPCs in the barrel and 18 in the endcaps. The RPCs allow the separation of muons and charged hadrons, and also detect penetrating neutral hadrons (mainly K_L).

The following sections provide more details on the subsystems of the detector together with current performance results.

3.1 Silicon Vertex Tracker

The Silicon Vertex Tracker (SVT) provides the required vertex resolution for the measurement of CP violation at PEP-II. In addition, it is capable of independent charged particle tracking, of particular importance for low transverse momentum particles ($p_T < 120 \text{ MeV}/c$) that cannot be measured by the central tracking chamber. The detector design is optimized to take into account the physical constraints imposed by the PEP-II geometry at the interaction region: the presence of

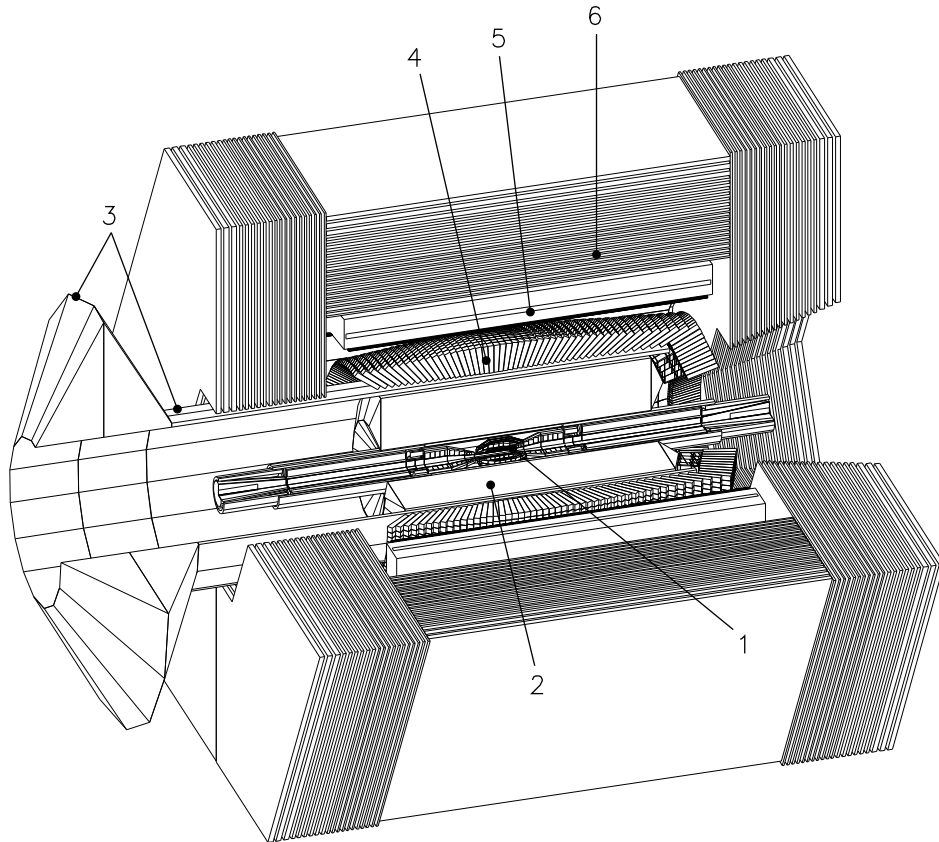


Figure 3: The *BABAR* Detector. 1. Silicon Vertex Tracker (SVT), 2. Drift Chamber (DCH), 3. Particle Identification Subsystem (DIRC–Detector of Internally Reflected Cherenkov Light), 4. Electromagnetic Calorimeter (EMC), 5. Magnet, 6. Instrumented Flux Return (IFR).

the B1 permanent magnets at ± 20 cm from the interaction point, which separate the beams after head-on collisions. The acceptance in polar angle θ is limited by the gap between beamline elements to $-0.87 < \cos \theta_{lab} < 0.96$ ($-0.95 < \cos \theta_{cm} < 0.87$). As the innermost *BABAR* subdetector, two important considerations in optimizing the design were low mass, to minimize multiple scattering, and radiation hardness of its components. A detailed description of the SVT and its components can be found in Ref. [4].

The SVT contains 52 modules built out of AC-coupled double-sided silicon sensors (strips orthogonal on the two sides). These are read out by a full-custom low-noise radiation-hard integrated circuit, known as the AtoM chip (mounted on a passive hybrid circuit that is attached to a water cooling channel). The detector modules are organized in five radial layers, each divided azimuthally into 6, 6, 6, 16 and 18 staves respectively (see Table 4). The three inner layers are crucial for vertex and tracking resolution, while the outer two layers are needed to provide additional measurements for stand alone tracking independent of drift chamber information. These outer two layers each contain two different types of modules, an inner (labelled *a* in the Table 4) and an outer (labelled *b*) layer, occupying slightly different radial positions. The modules are assembled on carbon fiber support cones, which in turn are positioned around the beam pipe and the B1 magnets. The SVT and some beamline elements are housed inside a strong support tube, with its load transferred at the ends to the PEP-II beamline support “rafts.”

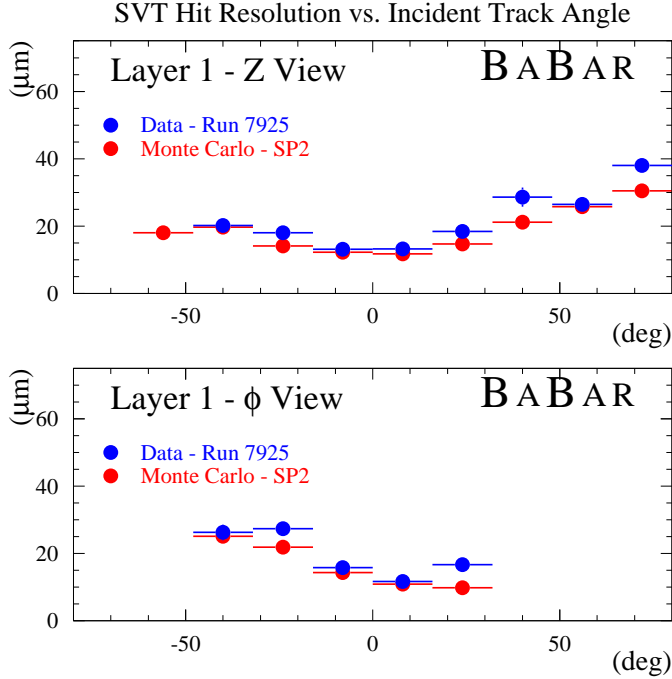


Figure 4: SVT single point resolution as a function of the incident track angle for the innermost layer.

Table 4: Layer Structure of the SVT.

Layer	Radius (mm)	Modules /Layer	Si Wafers /Module	ϕ pitch (μm)	z pitch (μm)
1	32	6	4	50 or 100	100
2	40	6	4	55 or 110	100
3	54	6	6	55 or 110	100
4a	124	8	7	100	210
4b	127	8	7	100	210
5a	140	9	8	100	210
5b	144	9	8	100	210

A system consisting of 12 PIN photodiode sensors is placed close to the first silicon layer to monitor continuously the radiation exposure of the SVT and manage its radiation dose budget.

During the first year of data taking, all major design goals for the detector were already achieved. The average hit reconstruction efficiency is above 98% in both views. The hit resolution presently observed, following an initial accurate alignment procedure, is shown in Figure 4. This compares well with Monte Carlo predictions for the resolution with perfect alignment. The impact parameter resolution, dominated by the SVT's precision for measuring high transverse momentum tracks, is

shown in Figure 5. Two-track vertices, such as $J/\psi \rightarrow \mu^+\mu^-$ are reconstructed with a typical resolution of $50 \mu\text{m}$; the resolution on the z separation between the two B decay vertices is typically $110 \mu\text{m}$, in good agreement with the design goals.

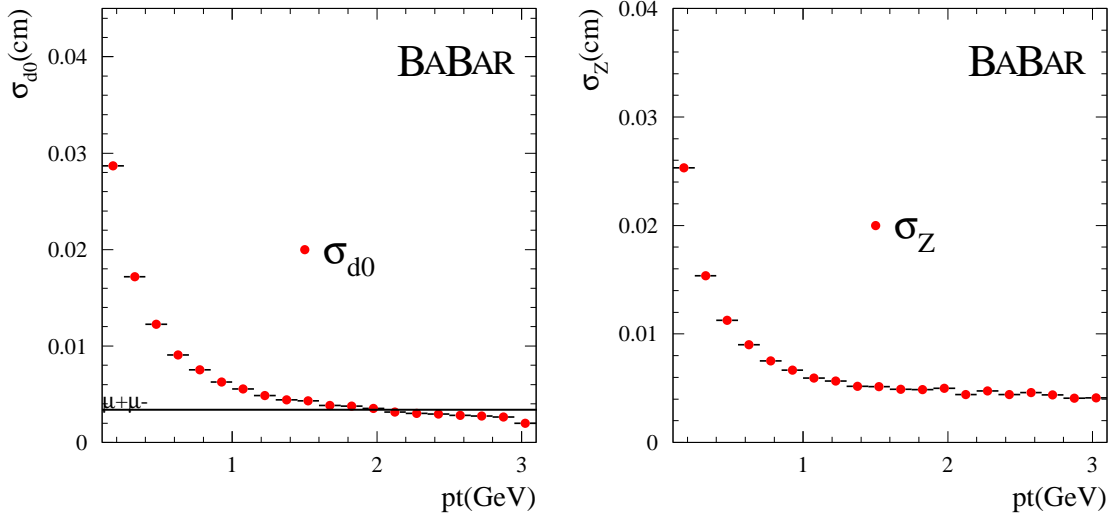


Figure 5: Impact parameter resolution in the $r - \phi$ (σ_{d0} in the left plot) and in the z -view (σ_z in the right plot) as measured on data. The horizontal line in the left-hand plot is $1/\sqrt{2}$ times the transverse miss distance for muon pair events.

3.2 Drift Chamber

The Drift Chamber (DCH) is the main tracking device for charged particles with transverse momenta p_T above about $120 \text{ MeV}/c$, providing a precision measurement of p_T from the curvature of charged particle trajectories in the 1.5 T magnetic field. Prompt single-cell hit information from the chamber is also a basic component of the Level-1 trigger (see Section 3.6.1). The DCH is a 280 cm -long cylinder, with a inner radius of 23.6 cm and an outer radius of 80.9 cm . It is mounted in cantilever from the rear endplate to the DIRC central support tube, within the volume inside the DIRC and outside the PEP-II support tube. The center of the chamber is displaced forward by 36.7 cm to improve the forward track length, given the asymmetric boost for the $\Upsilon(4S)$ events. The beryllium inner wall (0.28% radiation lengths), the thin outer half of the forward endplate (15 cm aluminum), and the carbon-fiber outer cylinder are all designed to minimize material in front of the calorimeter.

The drift system consists of 7104 hexagonal cells, approximately 1.8 cm wide by 1.2 cm high, arranged in 40 concentric layers between a radius of 25.3 and 79.0 cm . The active volume provides charged particle tracking over the polar angle range $-0.92 < \cos \theta_{lab} < 0.96$. The forty layers are grouped into ten superlayers of four layers each, organized with the same orientation for sense and field wires within a given superlayer. The superlayer structure facilitates fast local segment finding as the first step in pattern recognition. This arrangement is particularly important for Level-1 trigger decisions. Superlayers alternate in orientation: first axial (A), then a small positive stereo

angle (U), followed by a small negative stereo angle (V). All superlayers participate in the Level-1 trigger track finding; only the axial superlayers participate in the Level-1 trigger p_T determination.

Table 5: Layer arrangement for the DCH

Superlayer	Inner Radius [cm]	Cells/ Layer	Stereo Angle [mr]
1	26.04	96	0
2	31.85	112	+ [44.9–50.0]
3	37.05	128	- [52.3–57.4]
4	42.27	144	0
5	48.08	176	+ [55.6–59.7]
6	53.32	192	- [62.8–66.9]
7	58.54	208	0
8	64.30	224	+ [65.0–68.5]
9	69.52	240	- [72.1–75.8]
10	74.72	256	0

The individual hexagonal cells each consist of a $20\ \mu\text{m}$ rhenium-tungsten sense wire operating nominally in the range 1900–1960 V, surrounded by 6 cathode wires, approximately half of which are shared with neighboring cells. For the inner cells in a superlayer, the cathode wires are $120\ \mu\text{m}$ aluminum, grounded to the rear endplate. For outer cells one of the cathode wires is $80\ \mu\text{m}$ aluminum, held at about 350 V. All sense and cathode wires are gold plated. Table 5 summarizes the main geometric features of the design. The counting gas, chosen to have low mass, is an 80%:20% mixture of He:Isobutane, with a small amount (3000 ppm) of water vapor to prolong the lifetime of the chamber in a high rate environment. The combination of low-mass gas and minimization of material in the field cage itself is designed to reduce the contribution of multiple scattering to the p_T resolution for the typically soft tracks produced in $\mathcal{T}(4S)$ events.

The DCH readout electronics, including front-end amplifier, timing and pulse height digitization, event readout and high voltage distribution, are all mounted on the rear endplate (opposite the boost direction) to keep the additional material outside the detector fiducial volume. The instrumentation includes two custom integrated circuits: a low-noise bipolar amplifier IC and a CMOS digitizer IC that incorporates 8 channels of TDC, Flash-ADC, pipelined data-storage, multiple event buffers and prompt trigger output. Data readout is multiplexed on four fiber-optic links to *BABAR*-standard VME readout modules (ROM); trigger data is transported on 24 fiber-optic links. The ROMs extract the integrated charge from the digitized waveform before passing the data on to next level in the data acquisition system. High voltage is supplied by a CAEN SY527 mainframe and is distributed through circuit boards that plug directly on the DCH endplate feedthroughs. Temperature and humidity sensors monitor the chamber environment, and radiation monitors track the accumulated dose.

The nominal design for the chamber calls for an average $140\ \mu\text{m}$ single point resolution. The space-time relation (STR) for the non-saturated counting gas has been modeled with a separate 6th-order Chebychev polynomial for the left and right parts of the cell. The STR has proven to be very stable over time. There is a small residual dependence on gas density, not yet corrected in production. The single cell resolution function obtained from the ensemble of charged tracks in the

normal event stream is shown in Figure 6 for operation at 1960 V. This shows a weighted average resolution of $125 \mu\text{m}$.

In addition to recording timing information for hits, the Flash-ADC is used to measure the time development of pulse height in the cell. Signal processing (feature extraction) in the ROM converts this into a measurement of deposited energy. Real-time overall gain corrections are calculated and applied during the reconstruction step. Saturation, path length, polar angle, individual wire and layer gain corrections are applied as well, although these corrections are stable over long periods of time. The resulting distribution of the truncated mean dE/dx observed for Bhabha electrons is shown in Figure 6. The observed resolution is found to be 7.5%. We expect to achieve the predicted resolution of 7% after additional corrections, including the effect of varying entrance angles.

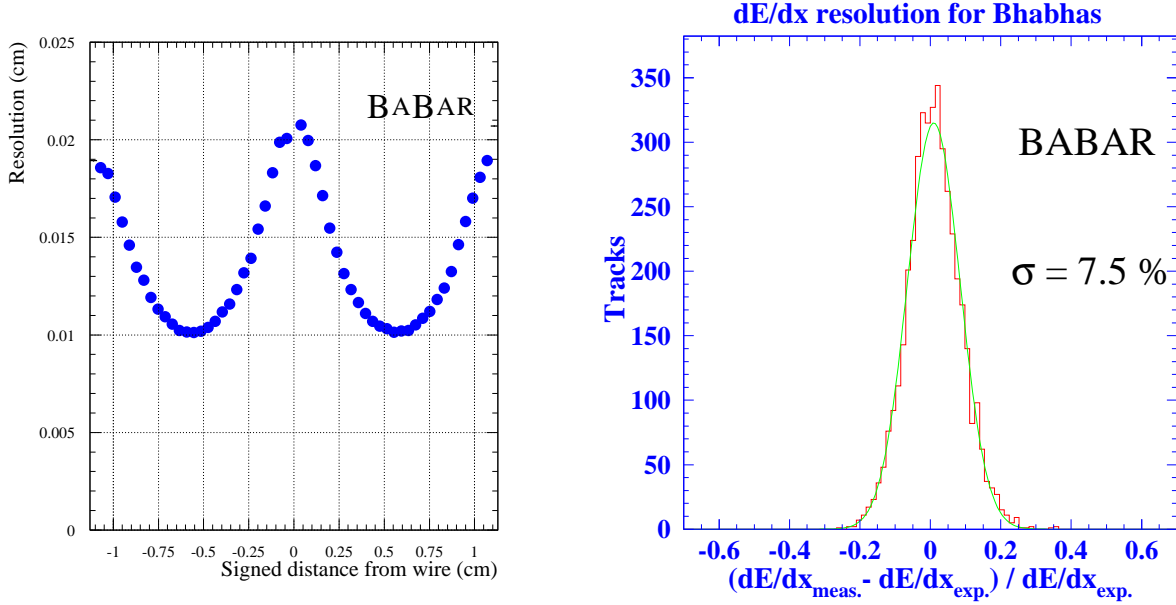


Figure 6: DCH single cell resolution (left) and dE/dx resolution for Bhabha electrons (right).

3.3 Particle Identification System

Standalone identification of charged particles is based on a specialized subdetector system that uses the Detection of Internally Reflected Cherenkov light (DIRC). Charged particles exiting the barrel region of the DCH transit an array of 144 fused silica quartz bars, each approximately 17 mm thick (δr), 35 mm wide ($\delta(r\phi)$) and 4.9 m long (δz). Particles above Cherenkov threshold radiate photons in the quartz media. The angles of the Cherenkov photons with respect to particle direction are measured with an array of 10,752 photomultiplier tubes located outside the return yoke, in a special low magnetic field volume. The polar angle coverage is $-0.84 < \cos \theta_{lab} < 0.90$.

The 144 quartz bars of the DIRC are arranged in 12 modules, or “bar-boxes”, that penetrate through the magnetic end plug. Cherenkov photons trapped in a quartz bar exit the bar through a wedge and a quartz window into a water tank, which optically couples the quartz bars to the photomultiplier array. The photomultiplier tubes are arranged in 12 sectors corresponding to the 12 barboxes, on the surface of a half torus, with a major radius of about 3 m and a minor radius of 1.2 m. By knowing the particle direction from the tracking system, and the location of the

photomultiplier tube that observes a Cherenkov photon, the angle that a Cherenkov photon makes with respect to the track direction can be deduced. Due to internal reflections within the bars, there are several solutions for a hit-to-track association. The angular resolution for a single photon is about 10.2 mr (see Figure 7(a)) and, with an average of 30 photons per track, the “per track” Cherenkov resolution is about 2.8 mr, rms. This corresponds to a separation of approximately three standard deviations between charged K ’s and π ’s at 3 GeV/ c . An additional observable is the time of a photomultiplier hit, measured to a precision of 1.7 ns (see Figure 7(b)). By comparison of the measured hit time with the propagation time of a photon solution, it is possible to effectively suppress background photons and invalid photon solutions.

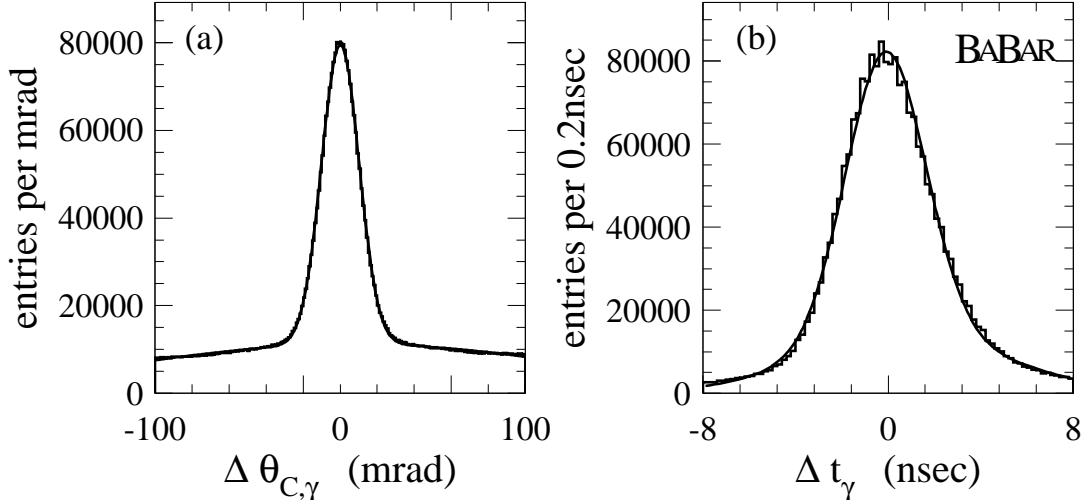


Figure 7: Resolution of the reconstructed Cherenkov angle for single photons (a) and of the difference between measured and expected arrival time (b).

3.4 Electromagnetic Calorimeter

The Electromagnetic Calorimeter (EMC) contains 6580 CsI crystals doped with thallium iodide at about 1000 ppm. Each crystal is a truncated trapezoidal pyramid and ranges from 16 to 17.5 radiation lengths in thickness. The front faces are typically ~ 5 cm in each dimension. The crystals are arranged quasi-projectively in a barrel structure of 48 polar (θ) rows by 120 crystals in azimuth (ϕ), with an inner radius of 90 cm. The forward end is closed by a separable endcap capable of holding nine additional rows. At present, eight are filled with crystals and the innermost with shielding absorber. The polar angle coverage of the calorimeter is $-0.78 < \cos \theta_{lab} < 0.96$. Beam-line elements occlude $\cos \theta_{lab} > 0.94$. Each crystal is wrapped with a diffuse reflective material (TYVEK) and housed in a thin eggcrate-like carbon fiber composite mechanical structure. There are 280 such modules in the barrel (7 types, 40 of each type) and 20 identical endcap modules. Crystals are read out with two independent 2 cm^2 large area PIN photodiodes epoxied to their rear faces. Dual-range ASIC preamplifiers reside directly behind the photodiodes in a shielded housing that also provides a thermal path for heat removal. Shielded ribbon cables carry analog signals to the end flanges of the barrel and the back plate of the endcap, where additional amplification

and digitizing electronics provide for a total of four overlapping linear ranges. The system handles signals from ~ 50 keV to ~ 13 GeV, corresponding to 18 bit dynamic range. A short shaping time of ~ 400 ns is used in the preamplifiers to reduce the impact of soft (< 5 MeV) beam-related photon backgrounds. Noise performance can be recovered by digitally processing the signal waveform sampled at 4 MHz. Calibration and monitoring is achieved by charge injection into the front end of the preamplifiers, a fiberoptic/xenon pulser system injecting light into the rear of each crystal, and a circulating radioactive source (a neutron-activated fluorocarbon fluid) producing a 6.13 MeV photon peak in each crystal. Signals from data (π^0 s, η s, radiative, and non-radiative Bhabhas, $\gamma\gamma$ and $\mu^+\mu^-$ events) can provide additional calibration points. Source and Bhabha calibrations are updated weekly to track the small changes in light yield with integrated radiation dose. Light pulser runs are carried out daily to monitor relative changes at the $< 0.3\%$ level.

The calorimeter has achieved an electronics noise energy (ENE) of ~ 220 keV (coherent plus incoherent) measured with the source system (in the absence of colliding beams) after digital signal processing. During regular data taking, this digital filtering is not applied and the ENE rises to ~ 450 keV owing to the short shaping time; consequently, only channels with > 1 MeV are presently used in the reconstruction of calorimeter energy deposits. The efficiency of the calorimeter exceeds 96% for the detection of photons with energies above 20 MeV.

The energy resolution can be measured directly with the radioactive source at low energies and with electrons from Bhabha scattering at high energies, yielding resolutions of $\sigma(E)/E = 5.0 \pm 0.8\%$ at 6.13 MeV and $\sigma(E)/E = 1.9 \pm 0.07\%$ at 7.5 GeV, respectively. The energy resolution can also be inferred from the observed mass resolutions for the π^0 and η , which are measured to be around 7 MeV and 16 MeV, respectively.

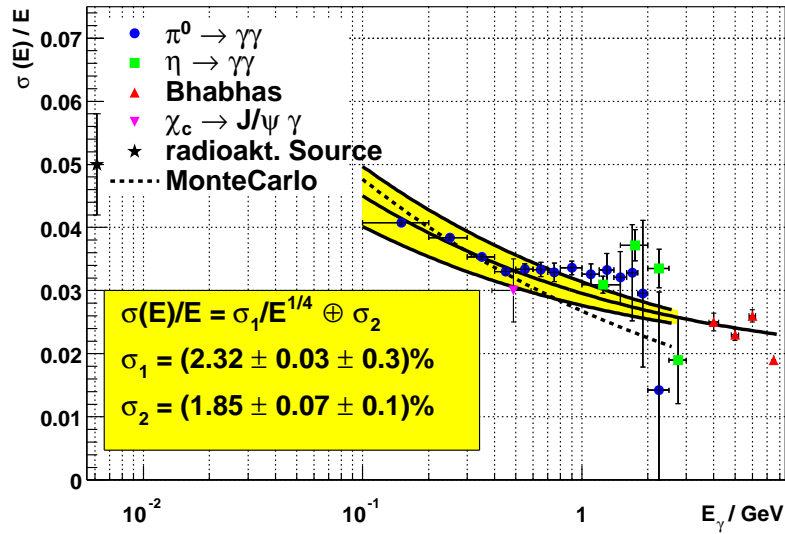


Figure 8: The energy resolution as a function of energy, as determined from the observed width of π^0 and η decays to two photons of equal energy, and the resolution for Bhabha electrons. The shaded band is the best fit to the π^0 , η , and Bhabha data. Also shown is the energy resolution of the 6.13 MeV photons from the radioactive source, and of the photons in the transition $\chi_{c1} \rightarrow J/\psi \gamma$.

Figure 8 shows the energy resolution extracted from a variety of data as a function of energy. A fit to the π^0 , η , and Bhabha energy resolution measurements, assuming an energy dependence of the form:

$$\sigma(E)/E = \sigma_1(E/\text{GeV})^{-1/4} \oplus \sigma_2, \quad (1)$$

gives $\sigma_1 = (2.32 \pm 0.30)\%$ and $\sigma_2 = (1.85 \pm 0.12)\%$. Implementation of digital filtering will reduce the electronics and beam background noise. This, together with the afforded improvements in cluster reconstruction algorithms, will lead to better energy resolution for the 2001 run, particularly at lower energies.

The π^0 and η data are also used to measure the angular resolution of the calorimeter. It is found to vary between about 12 mr at low energies and 3 mr at high energies, described by an energy dependence according to:

$$\sigma_{\theta,\phi} = \sigma_1(E/\text{GeV})^{-1/2} + \sigma_2, \quad (2)$$

with $\sigma_1 = (3.87 \pm 0.07)$ mrad and $\sigma_2 = (0.00 \pm 0.04)$ mrad.

The calorimeter is also used for the separation of hadrons from electrons, and in conjunction with the IFR for muon and K_L^0 identification; its performance in these areas is presented in section 7.2.

3.5 Instrumented Flux Return

The Instrumented Flux Return (IFR) is used to identify muons and neutral hadrons. The detector consists of nearly 900 Resistive Plate Chambers (RPCs) interleaved with the iron plates which comprise the flux return for the 1.5 T solenoidal magnet. There are 19 RPC layers in the barrel region and 18 layers in the forward and backward endcaps. The iron plate thickness is graded from 2 cm for plates closest to the interaction region to 10 cm for the outermost layers for a total of ≥ 65 cm in the barrel and ≥ 60 cm in the endcaps. An additional cylindrical RPC containing two layers is located in the barrel region between the calorimeter and solenoid cryostat.

The single gap planar RPC's [5] are constructed from 2 sheets of bakelite separated by 2 mm spacers. The inner surfaces are treated with linseed oil. The outer bakelite surfaces are painted with graphite. Layers of insulating mylar, aluminized mylar pickup strips, foam and an aluminized mylar ground-plane are glued to both sides of the bakelite forming the RPC package. The pickup strips are connected with discriminator cards which record a bit per strip if an in-time signal above threshold is recorded. The pickup strips on top and bottom are orthogonal, providing x-y position information in the endcaps and ϕ -z information in the barrel. The cylindrical RPC's are constructed from a special plastic requiring no surface treatment. The RPC's utilize a gas mixture of 56.7% Argon, 38.8% Freon-134a, and 4.5% Isobutane and operate at 7.6 kV. The cylindrical RPC's use the same gas but run at 7.4 kV. The steel flux return is water-cooled to reduce temperature excursions, keeping the barrel at $\sim 20^\circ\text{C}$ and the endcaps at $\sim 22\text{--}24^\circ\text{C}$.

The RPC efficiencies are measured in cosmic ray runs taken weekly and in collision data. The average chamber efficiencies during the 2000 run were $\sim 78\%$ in the barrel, and $\sim 87\%$ in the forward endcap, lower than the average $\sim 92\%$ measured in June 1999. A small fraction of the RPC's is presently disconnected because of high-voltage problems. A vigorous testing and R&D program is underway to understand the efficiency decrease and to improve RPC performance.

3.6 Trigger

The *BABAR* trigger system consists of the Level-1 hardware trigger and the Level-3 software trigger. The Level-1 trigger decision is issued within a latency of 11–12 μs after the corresponding beam crossing to initiate the Data Acquisition (DAQ) readout of the relevant time slice of the pipelined data for all detectors. The latency for hadronic events is confined to a smaller, $\pm 150\text{ns}$, range. The acquired data are processed by Level-3 running on the online farm nodes to select physics and calibration events for data logging.

3.6.1 Level-1 Trigger

The Level-1 (L1) trigger system comprises the DCH track trigger (DCT), the EMC energy trigger (EMT), the IFR muon trigger (IFT) and the global trigger (GLT). The L1 trigger system operates in a continuous sampling mode, processing input data and generating output trigger information at fixed time intervals. The main logic of the L1 trigger is implemented in six types of 9u VME modules with a total of 41 boards. The basic trigger primitives generated by the DCT, EMT and IFT, mostly ϕ maps of the particle signatures, are collected by the GLT to form 24 trigger lines for the fast control system. The DCT identifies short and long track primitives as well as high p_T track primitives. Using the loosest criteria, short tracks are accepted down to $p_T > 120\text{MeV}/c$ if they reach superlayer five in the DCH. The EMT generates trigger primitives passing various energy thresholds. The lowest threshold is 100 MeV, in order to be fully efficient for minimum ionizing particles.

All the L1 trigger system components appear to the data acquisition system as standard detector subsystems, in addition to their role in providing the trigger signals. The data read out from them provides details on the operation of the trigger for each acquired event, facilitating diagnostics and the determination of the L1 trigger efficiency.

The L1 trigger system is designed to be able to trigger independently from pure DCT and pure EMT triggers with high efficiency for most physics sources, in order to allow cross-calibration of efficiencies. In particular, $B\bar{B}$ events are triggered at $> 99\%$ efficiency from either DCT or EMT and the combined efficiency is $> 99.9\%$. Only τ and two-photon events do not have a fully efficient pure EMT trigger and rely mainly on DCT triggers.

The total L1 trigger rate for a typical run with HER (LER) currents at 700 mA (1100 mA) and a luminosity of $2.0 \times 10^{33}\text{cm}^{-2}\text{s}^{-1}$ is $\sim 700\text{ Hz}$. This is typically stable to within 10% for the same machine currents but can be 50% higher after a major shutdown when the vacuum is relatively poor. The joint trigger/data acquisition system rate capability is comfortably beyond the design rate of 2 kHz. This avoids significant deadtime, and leaves room for the expected increase in luminosity. Within the typical L1 trigger rate of 700 Hz at $2 \times 10^{33}\text{cm}^{-2}\text{s}^{-1}$, Bhabha events and other e^+e^- interactions amount to around 120 Hz, and cosmic ray interactions to 130 Hz. The dominant source of background causing the remaining triggers is the interaction of lost particles with the beam line components. The L1 background rate coming from the HER beam is ~ 3 times higher than that from the LER beam for the typical operating currents.

3.6.2 Level-3 Trigger

The Level-3 (L3) trigger is the first component of the trigger system to see complete events. It is embedded in the Online Event Processing (OEP) framework running in parallel on 32 event filter farm nodes. The L3 trigger processes data from the DCH track trigger and from the EMC using

two independent algorithms that form track and cluster objects. These are fed into a set of filter algorithms that operate on either one or both. The L3 DCH algorithm performs fast lookup-table based track finding and three-dimensional track fitting, efficient for tracks with $p_T > 250$ MeV/ c . The *event* t_0 is determined from DCH trigger track segments and hit data to better than 5 ns. The L3 EMC algorithm uses calorimeter crystal data in a fast two-dimensional clustering algorithm implemented using a lookup table. To reduce noise, the crystal energy threshold is set to 30 MeV. L3 clusters are accepted for energies > 100 MeV.

The L3 logging decision is based on generic track/cluster topologies rather than on the identification of individual physics processes. An exception is made for Bhabha events, which have to be vetoed to reduce their rate (~ 100 Hz at 2×10^{33} cm $^{-2}$ s $^{-1}$ luminosity). The physics trigger is a logical OR of two orthogonal filters. The track filter requires either one track with $p_T > 800$ MeV/ c coming from the interaction point, or two tracks with $p_T > 250$ MeV/ c and slightly looser vertex cuts. The cluster filter accepts events with a high multiplicity or with a large total energy in the EMC and a high invariant (pseudo) mass. The efficiency of the track filter for $B\bar{B}$ events is 99%, while the efficiency of the cluster filter is 94%.

Both filters are subject to a veto algorithm that identifies Bhabha events based on clean signatures in the DCH and the EMC. The veto has no impact on hadronic events, and only has noticeable effect on very few types of events such as $\tau\tau \rightarrow e\nu e\nu e\nu$. A prescaled sample of Bhabha events, flattened in θ , is preserved for calibration purposes. In addition, L3 logs various other samples for calibration and monitoring, such as radiative Bhabha events, cosmics, and random triggers. The luminosity is measured online by L3 using a track-based algorithm with a scale calibration precision of $< \sim 5\%$. The typical logging rate at 2.0×10^{33} cm $^{-2}$ s $^{-1}$ is ~ 85 Hz, well within the design specifications.

3.7 Data Acquisition and Online System

The *BABAR* data acquisition system employs a set of standard Readout Modules (ROMs) to communicate with the front-end electronics of the detector systems. A common communications fabric—1 Gbps optical fiber links—and protocol is used for readout by all the systems, with detector-specific extensions to the protocol for control.

Each ROM is built around a commercial VME single-board computer running VxWorks, linked with three custom boards, one of which supplies one of two “personalities”. The calorimeter uses an untriggered version of the ROM which continuously collects data from up to three input data fibers, separating out in software the data corresponding to L1 triggers. All of the other detector systems use a version which requests and collects event data from up to two fibers upon the receipt of a L1 trigger.

ROMs are organized into crates in groups of two to eleven, including a master ROM. The master builds partial events from the data acquired by the crate’s other ROMs from the front ends. Final event building is performed by sending these data fragments via 100-Mbps switched Ethernet to the nodes of the Online Event Processing (OEP) farm, which are commercial Unix workstations. Static load-balancing is used, allocating events to nodes using a simple deterministic algorithm based on a unique time stamp assigned to each L1 trigger.

The farm nodes in OEP apply the L3 trigger algorithms and perform fast data quality monitoring functions. Events passing the L3 selection are sent via TCP/IP to a single server process which logs them to disk files. Data quality monitoring results are collected from all nodes and merged for display to operators and for automated comparison against defined references.

This system has easily exceeded its fundamental performance requirement of acquiring 2000 Hz of L1 triggers and logging L3 triggers at up to 100 Hz. In recent running we have been operating far from its limits, with a L1 rate of approximately 700 Hz, an average event size of 27 kB, and a L3 logging rate of 85 Hz. There is therefore considerable headroom already available for operation at higher luminosities, but the system can be scaled further, if necessary, up to the data bandwidth limits of the front-end electronics through the addition of more ROMs and more OEP nodes.

The online computing system includes several additional components. The Detector Control system, which monitors and controls the experiments environmental systems such as low and high voltage power and detector gas supplies, as well as monitoring parameters of the PEP-II collider. The Run Control subsystem coordinates the activities of all the online and data acquisition components, and interlocks data acquisition with the maintenance of safe and acceptable detector and collider conditions.

3.8 Online Prompt Reconstruction

The first stage of production processing after data acquisition, the Online Prompt Reconstruction or OPR, is performed automatically by a compute farm which currently consists of about 150 Unix processors. All colliding beam events are filtered and tagged. Interesting events are completely reconstructed and written to the object database. A novel system of “rolling calibrations” extracts updated reconstruction constants from the data which are then written to the object database and used for subsequent reconstruction. Finally, detailed monitoring distributions are generated and fed back into the experiments data quality monitoring program.

OPR is designed and sized to keep up with the data acquisition with minimum latency. Typically, this latency between data availability and processed data is in the range from one to four 8-hour shifts. Thus, the system operates 24 hours per day and seven days per week.

A second, identical farm of processors is used for data reprocessing. Using the same mechanisms as OPR, the reprocessing system is used to reprocess older data once newer code or improved constants become available.

3.9 Computing System

The *BABAR* computing system includes the online system components described above, plus the computing required for offline reconstruction, simulation and analysis. This is implemented on several hundred commercial Unix computers (currently running Solaris, Linux and OSF operating systems), functionally distributed, with tcp/ip-based networking. Fileservers with RAID disk arrays and access to HPSS-based mass tape storage in STK robots are used to store and serve the data. Network switching employs Cisco technology both online and in the SLAC computing center.

The *BABAR* software is mostly C++, designed with OOAD methodology. A commercial database, Objectivity, is used for data and condition storage. Code distribution employs *BABAR*-developed release tools built upon CVS and the AFS distributed file system. The LSF batch scheduling system is used at the SLAC site. Data distribution to remote sites uses a combination of WAN, DLT7000 and Redwood/Eagle tapes. Data acquisition and reconstruction is performed at SLAC. Simulation and data analysis tasks are shared between SLAC and remote sites. These remote sites include major centers in France, Italy, UK and USA.

4 Data Sample

Results for this Conference are based on data collected up to July 6, 2000, when the total integrated luminosity recorded by the experiment was 12.7 fb^{-1} . Of this sample, 11.3 fb^{-1} was taken “on peak”, near the peak of the $\Upsilon(4S)$ resonance, and 1.4 fb^{-1} was taken “off peak” at a center-of-mass energy 40 MeV below the resonance. For the Osaka conference, the physics analyses are based on a sample of 8.9 fb^{-1} , of which 7.7 fb^{-1} is on peak and 1.2 fb^{-1} off peak. An additional 1.1 fb^{-1} of on-peak data was used in the analysis for $\sin 2\beta$, for a total of 10.0 fb^{-1} .

The remaining 2.7 fb^{-1} of recorded data falls into two categories. Data taken during the period between June and October 1999 (1.3 fb^{-1}), when the DIRC system was incomplete (only 5 of the 12 bar boxes were installed) and various subsystems were still optimizing their operation, will be of limited use for future physics analyses. Some data (1.2 fb^{-1}) was excluded from the Osaka sample because optimal alignment constants were unavailable when it was processed initially. This data will be available after reprocessing in August 2000.

4.1 Delivered and Recorded Integrated Luminosity

The luminosity is monitored by PEP-II and by *BABAR* in the trigger and prompt reconstruction. The L3 trigger calculates the deadtime, which is typically less than two percent. It also measures the luminosity from Bhabha events. The offline determination (described in Section 8.4) uses dimuon and two-photon events as well for cross-checks. The DAQ efficiency is monitored closely and is typically greater than 95%. Occasional scans of the resonance are used to make sure that the experiment is running on the $\Upsilon(4S)$ peak.

4.2 Off-Resonance Running

By running below the $\Upsilon(4S)$ resonance, *BABAR* can study the non- $B\bar{B}$ contribution on-peak. This is used to count the number of observed $B\bar{B}$ (see Section 8.5) and for background subtraction in many analyses, especially inclusive measurements. The amount of luminosity devoted to off-peak running is of less importance for clean channels like $B^0 \rightarrow J/\psi K_s^0$. The uncertainty of a measurement with a ratio of signal plus background to signal b depends [12] on the fraction of continuum luminosity c running as:

$$\sqrt{\frac{c+b}{c(1-c)}} . \quad (3)$$

For an analysis with $b = 0.02$, collecting about 12% of luminosity off-peak is optimal. This was the goal for the year 2000 run, which concentrates on measuring $\sin 2\beta$. As more luminosity becomes available, a somewhat higher rate of continuum running may be chosen to improve the background subtraction for modes like $B^0 \rightarrow \pi^+\pi^-$.

Operationally, the off-peak running took place about once a month. This minimized the amount of time spent tuning the machine after changing the beam energy, while still allowing the analyses to track changes in machine backgrounds, reconstruction code, and detector performance. The center-of-mass energy was reduced by lowering the HER energy by about 70 MeV, giving a center-of-mass energy of 10.540 GeV. The LER energy was left unchanged for simplicity’s sake; the resulting decrease in boost was negligible for all analyses.

4.3 Data Quality

Data quality is checked at each stage from the trigger to the analysis skims. Gross hardware problems, such as power supply failures or trips, are rare and are easily identified by the extensive slow control system. A member of the shift crew is assigned to monitor histograms, which are updated live with occupancy, timing, event size, and other performance information from the L1 and L3 triggers, the detector subsystems, and special online event processing cross-checks. Automatic processes test additional live histograms and report anomalies to the shifter or subsystem expert. This insures that problems are identified and fixed as soon as possible. Several subsystems also employ automated processes that perform tests on the data files to make long-term strip charts of the kind of information listed above.

The reconstruction job contains many histograms for each subsystem (including particle identification, beamspot and alignment monitoring, and results from some basic analyses). A subset is inspected by subsystem experts for each run. The most important quantities are extracted from the histograms to make charts showing the long-term behavior of the detector and reconstruction code, allowing detection of changes that are too subtle or gradual to notice on a run-by-run basis. The quality assessments from live data taking, online processing, and first-pass offline analysis are combined to define lists of good runs for further analysis. The yield per unit luminosity versus run for each skim is inspected to insure that the data used in physics analyses is of consistent quality within samples. Less than one percent of data was declared unusable by this process.

5 Simulation

The full detector simulation is structurally divided into three parts: event generation, the tracking of particles through the detector, and the detector response simulation.

5.1 Event Generators

The simulation process begins by generating events using one of several possible event generators. The beam energies used in the simulation are thrown using a Gaussian distribution of width 5.5 and 2.7 MeV for the high and low energy beams respectively. A transverse momentum spread of 2.8 and 1.3 MeV/ c , obtained from beam emittances for the HER and LER respectively, is also simulated. The position of the interaction point is modeled as a Gaussian distribution having widths of 125 μm , 4.2 μm , and 0.85 cm, in the x , y , and z directions respectively. The direction of the simulated beam axis is rotated with respect to the *BABAR* detector coordinate system by -18.8 mr in the y direction, as observed in data.

The main generator for $B\bar{B}$ physics is called `EvtGen`, details of which can be found in [6]. This generator provides a framework in which specific decay models can be implemented as modules. These modules can perform a variety of different functions such as calculating amplitudes for the decay. `EvtGen` introduces mixing by generating decays of the $\Upsilon(4S)$ to the proper mixture of $B^0\bar{B}^0$, \bar{B}^0B^0 , and B^0B^0 final states, with the correct distributions in Δt . CP asymmetries are generated in modules that modify the generated lifetime distributions of the two B 's produced in the decay of the $\Upsilon(4S)$. Generic models are available for simulating two-body decays to a pair of scalar mesons, a scalar and a vector meson, a scalar and a tensor meson, or a pair of vector mesons.

A main decay file is used (`DECAY.DEC`) which provides a fairly complete table of the decays of particles below the $\Upsilon(4S)$ to exclusive final states. For generic decays of B mesons, about 50% are generated to exclusive states, while the other 50% are produced using `Jetset7.4` fragmentation

model. `Jetset7.4` is also used to generate the $c\bar{c}$ states and weakly decaying baryons. The original `Jetset7.4` decay table was modified in order to be in line with recent measurements.

5.2 The GEANT3 Model

`BBsim` is based on the detector description and simulation tool, `Geant321` [7], developed at CERN. `Geant321` provides tools to construct the detector geometry; to step charged and neutral particles through the detector; to simulate the full variety of interactions and decays that each particle species may undergo; to register Monte Carlo track hits (referred to as GHits in *BABAR* terminology); and to display the detector components, particle trajectories and track hits.

`BBsim` is organized as a set of subsystem packages, each consisting of a standard set of routines which are called at various stages of the event simulation. In the initialization phase, the detailed subsystem geometries are built from parameters specified in an ASCII geometry database. The model includes the definition of the shapes, positions and orientations of all the subdetector components, and of the materials used in their construction.

Long-lived particles (“primaries”) produced in the event generation stage are stepped through the detector and allowed to interact or decay. In `BBsim`, hadronic interactions may be simulated using either `Gheisha` [8] (default), `Fluka` [9] or `GCalor` [10]. Secondaries resulting from interactions or decays are tracked as well. However, when recording the `Geant3`-level genealogy, only the kinematics of primaries and secondaries resulting from decays are included.

Particle GHits are scored in the active detector components. The GHit contains all the information needed to perform the subsequent detector response simulation, such as the position of the hit, the direction the track is traveling in, the energy lost, and the Monte Carlo track number. All of subsystem GHits are written to an output file, along with the generator- and `Geant321`-level Monte Carlo event generation information.

5.3 The Detector Response Simulation

The digitization of track hits is done as a separate step called `SimApp`. This uses the GHit information as input and outputs digitized data in the same format as the real detector. At the end of this stage the Monte Carlo data is processed by the same code that is run on the real data. The code is again organized as a set of subsystem packages. These packages contain routines to make the simulated data as realistic a match as possible to data taken by the detector. As an example, the drift chamber package takes account of the hit efficiencies measured using real data. Several figures showing the quality of the agreement between simulation and real data can be found in this paper.

Another function of the code in the `SimApp` packages is to add in background hits. Rather than simulate the backgrounds in the detector, events from samples recorded with random triggers are overlaid (using the appropriate luminosity weighting factor) with Monte Carlo simulated events.

Simulation production takes place at SLAC and at remote sites. The rate of production has been increasing with time and currently the level is about three million events a month. Since background data is used in the simulation, and the backgrounds in the machine fluctuate, some care is needed to ensure that the Monte Carlo is produced with representative backgrounds. Each production block corresponds to about a month of real data and uses background files and detector efficiencies “typical” of that month. The background events are shuffled to ensure that even small Monte Carlo data sets are generated with a sample of background events spread out over the entire time period.

6 Tracking and Vertexing

6.1 Track Finding and Kalman Filtering

Charged track finding in *BABAR* reconstruction starts with pattern recognition in the DCH. A better event time is needed than that available from the L3 trigger, so the first step is to find an improved t_0 using three parameter fits (d_0 , ϕ_0 , t_0) to four-hit track segments in the DCH superlayers.

The first pass at DCH track finding takes the track parameters and associated lists of hits from the output of the L3 track finder and performs helix fits; if a fit succeeds, that track is retained. A search for additional hits in the DCH that may belong on these tracks is made, and the event time is further refined using the timing information of just the hits assigned to tracks. Two subsequent track finders are run on the remaining DCH hits. Both track finders work on superlayer segments constructed out of hits not used on previous tracks, and are designed to find tracks at lower p_T than found by the L3 trackfinder, to find tracks going through fewer than the full ten superlayers, and to find tracks without bias towards the interaction point. In this way more sophisticated track finders run in a progressively cleaner tracking environment with a constantly improving measure of the event time.

At the end of this process, the found tracks are refit using a Kalman filter fitter. [11] This fitter takes into account the detailed distribution of material in the detector and the full map of the non-uniformities in the detector magnetic field. The tracks are then projected into the SVT, and silicon strip hits are considered for addition to the tracks if they are consistent with the expected error from extrapolating through the intervening material and field. Various possible combinations (branches) of SVT hits are considered, and the branch contributing the least to χ^2 , while meeting pattern requirements designed to limit the number of silicon wafers providing no measurement, is retained. When all intersected wafers have been inspected for hits and the best branch is selected, a full Kalman fit is performed on the ensemble of DCH and SVT hits.

Then a search for tracks is performed using the remaining unused silicon strips, as described in the next section. At the end of the SVT-only track finding, a search of the track list is made for tracks made up of only SVT hits which match closely at the support tube to other tracks made up of only DCH hits, since the support tube is a localized source of scattering between the two devices. If any candidates are found, a common fit to both sets of hits is attempted. If this succeeds, only the combined track is retained; otherwise, both stand-alone tracks are kept on the track list. At the end of pattern recognition and fitting, all tracks are checked to see if they lie in momentum ranges where the particle hypothesis might effect the result of the fit, and if so, each track is fit with up to five stable-particle mass hypotheses.

6.2 Tracking Efficiency

The absolute level of track reconstruction efficiency has been determined by studies using control samples from data. Changes in the DCH operating point and the reconstruction code during data taking are also followed in this way. The polar and azimuthal angle dependence of the track finding efficiency is modeled through detailed tuning of the Monte Carlo simulation. The overall level of track reconstruction efficiency and its dependence on angle or p_T is checked using:

- Bhabha scattering events at low multiplicity and high p_T ; events are selected based on calorimeter information and the efficiency for finding the e^+e^- tracks determined;
- one-versus-three tau-pair events at moderate multiplicity and p_T ranging up to about 2 GeV/ c ;

events are selected without requiring the third track on the 3-prong side, allowing a determination of the probability for reconstructing this track with a variety of track selection requirements;

- events containing a $D^0 \rightarrow K^- \pi^+ \pi^+ \pi^-$ decays where the D^0 is reconstructed from the decay $D^{*+} \rightarrow D^0 \pi^+$; the relative tracking efficiency for tight or loose requirements on the DCH portion of the track can be determined, as well as absolute efficiencies using the ratio of $D^0 \rightarrow K^- \pi^+ \pi^+ \pi^-$ to $K^- \pi^+$;
- multiplicity distribution of clean multihadron event selections;
- comparisons between standalone tracking in the SVT and DCH.

We assign a conservative 2.5% systematic error per track to the absolute track finding efficiency above 200 MeV/c in p_T in computing all branching fractions reported at this conference, and treat this as fully correlated for all studies that require a DCH portion of the track. This represents the level of consistency among track finding efficiency studies done so far, but in no way reflects the final systematic error that we expect to achieve with the tracking system.

6.3 Slow Pion Reconstruction

The tracking system in *BABAR* was designed to be highly efficient even for very low momentum tracks, which are important for reconstructing decays such as $D^{*+} \rightarrow D^0 \pi^+$ for which the π^+ has a very soft momentum spectrum. Tracks with transverse momentum (p_T) below about 120 MeV/c can not be found with the DCH pattern recognition because they curl up and do not penetrate deep into the DCH, which has an inner radius is 24 cm. The five-layer SVT was designed to be a stand-alone tracking device covering specifically the entire p_T range of 50–120 MeV/c. The lower p_T limit of 50 MeV/c is the threshold below which pions have a large probability of stopping in the material of the beam pipe.

The SVT stand-alone pattern recognition is performed by two independent algorithms after SVT hits have been associated with, and claimed by, stand-alone DCH tracks. The first algorithm builds tracks from space points, which are intersections of ϕ and z strips. The second algorithm forms circle trajectories with the ϕ hits and then adds z hits to the circles to form helices. The first algorithm is efficient over a wide range of impact parameter and z_0 values but is susceptible to inefficiencies in events with an extremely large number of hits and from silicon modules with non-functional sides (ϕ or z). The second algorithm is less sensitive to extreme combinatorics and module defects and is used to find tracks missed by the first algorithm.

Figure 9 shows the slow pion p_T spectra from the decay $D^{*+} \rightarrow D^0 \pi^+$, after subtraction of combinatorial background using the $m(D^0)$ sidebands, for on-resonance data and a mixture of $b\bar{b}$ and $c\bar{c}$ Monte Carlo which represents the on-resonance conditions. The shape of the p_T spectra agree quite well, which gives us some confidence in our Monte Carlo simulation. Figure 9 also shows the tracking efficiency as a function of p_T as derived from the Monte Carlo. The efficiency turns on at a p_T of about 50 MeV/c and crosses 80% at about 70 MeV/c. We have tried to measure the relative tracking efficiency at low momentum from the data alone using slow π helicity distributions, binned in $p^*(D^{*+})$. Currently, this measurement is statistically limited, but will eventually yield a tracking efficiency measurement at low momentum from the data without Monte Carlo dependence. We assign an uncorrelated 2.5% systematic error to the track finding efficiency for those tracks that rely on the SVT only.

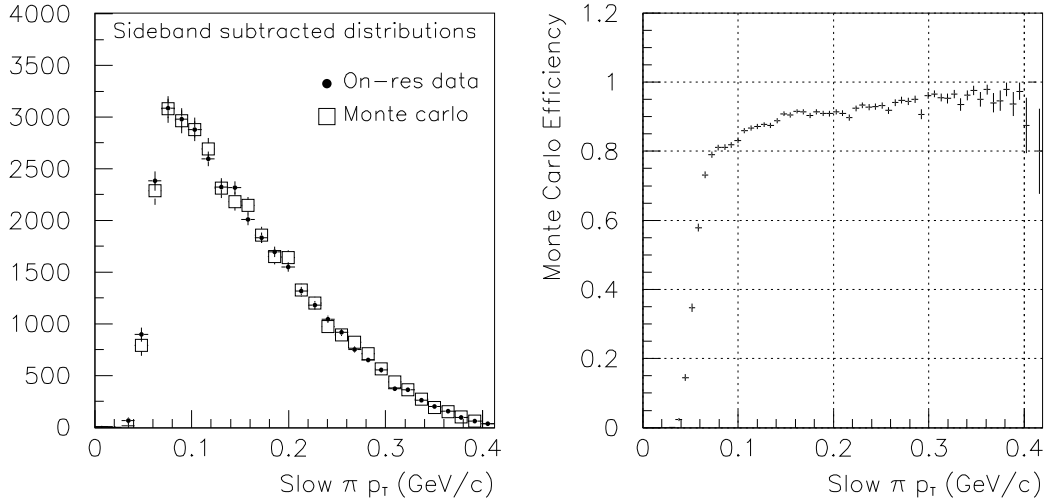


Figure 9: The figure on the left shows the slow pion p_T spectrum, after subtraction of combinatorial background using the $m(D^0)$ sidebands, for on-resonance data (points) and Monte Carlo (boxes). The plot on the right shows the tracking efficiency as a function of p_T derived from the Monte Carlo.

6.4 Vertex and Kinematic Fitting

Vertex and kinematic fitting is widely used to improve four-momenta and position measurements, as well as to measure the time difference between decaying B hadrons in the $\Upsilon(4S) \rightarrow B\bar{B}$ decay. Combined with tracking and particle identification, vertex and kinematic fitting provides the basis for event identification.

The physics properties of a decay are used to apply constraints which translate to better mass and position resolutions and larger signal-to-background ratios. For example, in the case of $B^0 \rightarrow J/\psi K_S^0$, the position measurement of the B^0 can be improved using the fact that the line-of-flight of the K_S^0 intersects the J/ψ vertex. The energy resolution of the B^0 can also be improved by applying a mass constraint to the J/ψ . Several constraints have been implemented utilizing the Lagrange Multiplier mechanism [15]: common decay vertex, mass, energy, momentum, beam energy (with and without smearing), beam spot position and line-of-flight. In all cases constraints are applied in three dimensions.

One of the fundamental principles in the design was to deal in a simple way with complex decay chains. Virtual *composite* particles and their error matrices are built from the original particles. The composite particle then replaces the daughters in subsequent fits and analysis. To account for intermediate resonances and neutral particles, vertices can be shared by different virtual states. The three-momentum of the virtual particle is fit directly, rather than computed from the updated daughters, improving speed and numerical accuracy.

Non linearities in the fits require the application of an iterative procedure. Simple fits involving only vertex constraints (except long-lived particles, called V^0 's) are, however, accurate enough with a single iteration. This has an important impact on the amount of time consumed in vertex fitting. The other fits involving kinematic constraints and V^0 's require, in general, more than one iteration.

The criteria we use for convergence is that the change in χ^2 between two successive iterations is less than 1%, with a maximum of six iterations. In all cases the initial location of the vertex is estimated by solving analytically (with an iterative procedure) the point of closest approach of the two tracks, using a second-order approximation at each point.

Track and vertex parameter errors depend heavily on our understanding internal and global alignment, detector material, and magnetic field variation. A set of control samples ($\gamma\gamma \rightarrow 4\pi$, $\tau \rightarrow 3\text{-prongs}$, $D^0 \rightarrow K^-\pi^+\pi^-\pi^+$, $B^- \rightarrow J/\psi K^+$) has been used to estimate from data the vertex position and mass resolutions and systematic uncertainties in their determination. The pull distributions of these control samples show that tracking and vertex errors are estimated correctly at the 10–20% level and that biases in determining vertex positions due to alignment problems are at the level of a few microns.

6.4.1 Beam spot and primary vertex determination

In order to accommodate the movements of the PEP-II beam with respect to the *BABAR* detector, the position of the collision point at PEP-II is determined from track-based methods. The apparent size from two-prong events is about $150\ \mu\text{m}$ in x , $50\ \mu\text{m}$ in y and 1 cm in z . The apparent size in the y direction is totally dominated by the track resolution. A better estimate of σ_y can be obtained from the knowledge of the luminosity, the beam currents and the size in x , providing a value of about $4\ \mu\text{m}$, varying within 10% on a time scale of hours.

For many physics analyses and reconstruction tasks, it is necessary to have a more accurate estimate of the collision point in x and z . For instance, reconstruction of γ and π^0 candidates uses, in many cases, the primary vertex as the point of origin in reconstructing vectors. The primary vertex³ is estimated on an event-by-event basis from a vertex fit which uses charged tracks with an impact parameter (with respect to the beam spot position) less than 1 mm in the transverse plane. Tracks with high χ^2 contribution to the vertex fit are removed until an overall χ^2 probability greater than 1% is obtained. The resolution is about $70\ \mu\text{m}$ in x , y and z for hadronic events.

6.4.2 Reconstruction of the tagging- B vertex

In measurements of the B lifetime, mixing rate and time-dependent CP -violating asymmetries, we fully reconstruct or partially reconstruct only one B and then determine the distance between the two B decays. Determination of the fully-reconstructed B decay vertex makes use of all the final-state tracks of the B decay chain. The other B vertex (tagging- B vertex) is reconstructed with the remaining charged tracks in the event. To retain high efficiency this is done with inclusive techniques. Complications arise from the fact that one has to deal with secondary tracks from short- and long-lived particles. To deal with these problems and minimize their impact, the three-momentum of the tagging- B (called a pseudo-track) and associated error matrix are derived from the three-momentum, decay vertex and error matrix of the fully reconstructed B candidate, and from a knowledge of the average position of the interaction point and the $\mathcal{T}(4S)$ four-momentum. In the case of partial B reconstruction (where the three-momentum is not known) the constraint from the B pseudo-track cannot be used. This pseudo-track is fit to a common vertex with the remaining tracks in the event. Reconstructed V^0 candidates are also used in this procedure, reducing biases from long-lived decay particles. Tracks with contributions to the χ^2 greater than six are removed

³ For light quark events, the reconstructed vertex is a good estimate of the true primary vertex. For $B\bar{B}$ events, where both B mesons travel along the z axis in the laboratory frame, the primary vertex provides an average B decay position.

from the fit. The procedure is iterated until there are no tracks contributing more than six units to the χ^2 or all tracks are removed.

The Δz resolution function obtained with this technique can be accurately described by the sum of two Gaussian distributions with different means and widths. Typically, 80% of the events are in the core Gaussian, which has a width $\approx 100 \mu\text{m}$. The remaining events reside in the tail Gaussian which has a typical width $\approx 350 \mu\text{m}$. The bias due to secondary tracks is $\approx -20 \mu\text{m}$ for the core Gaussian and $\approx -80 \mu\text{m}$ for the tail Gaussian. An inclusive $D^{*-} \rightarrow D^0 \pi^-$ control sample (selected from continuum and off-resonance running) is used to check the Δz reconstruction and resolution for data.

7 Particle Identification

7.1 Charged Particle Identification

7.1.1 Electrons

Electrons are identified with the EMC, the DCH and the DIRC systems, using quantities such as the ratio of the deposited energy over the momentum, and variables describing the spatial shower development. The lateral shower development is measured with a method introduced by ARGUS [16] and expanded into various moments containing information about the shower's azimuthal distribution with respect to the particle's initial momentum [17]. A cut is applied on the energy loss using a truncated mean of 40 samples (maximum) recorded in the DCH. The measured Cherenkov angle in the DIRC is required to be within 3σ of the expected value for the electron hypothesis. The efficiency of electron identification is studied by using electrons obtained from radiative Bhabhas and events of the process $\gamma\gamma \rightarrow e^+e^-$. The misidentification probability for pions is measured with 3-prong τ decays. The *tight* selector has an average efficiency of 94.8% in the momentum range $0.5 \text{ GeV}/c < p < 2 \text{ GeV}/c$, with a pion misidentification probability of roughly 1.2%. The *very tight* selector has an efficiency of 88.1% with an average pion misidentification of 0.3%. The dependence of the efficiency on momentum and polar angle is shown in Figure 10.

7.1.2 Muons

Charged tracks reconstructed in the DCH are extrapolated to the flux return iron using a detailed map of the non-uniform magnetic field and accounting for the expected average energy loss. The predicted average position of the intersections with the active detector planes is computed, including the uncertainty due to multiple scattering. All hits found in each readout view within a specified maximum distance from the predicted intersection are associated with the charged track. We require, for tracks within the acceptance of the EMC, the energy deposition to be consistent with that expected of a minimum ionizing particle. A signal in at least two layers of the IFR is also required. A cut is also made on the difference between measured and predicted (based on the muon hypothesis) total number of interaction lengths traversed in all subdetectors. We expect the average number of signal strips per layer to be larger for pions produced in an hadronic interaction than for muons. The average value and the r.m.s. of the strip pattern for the different hit layers provides μ/π discriminating power. Finally, we reject tracks with a large track-match χ^2 or a large χ^2 for a polynomial fit to the IFR cluster.

The performance of the muon selectors has been tested using control samples obtained from data. The processes considered are $\mu\mu e e$ and $\mu\mu\gamma$ for muons, and $\tau \rightarrow 3\text{-prongs}$ and $K_S \rightarrow$

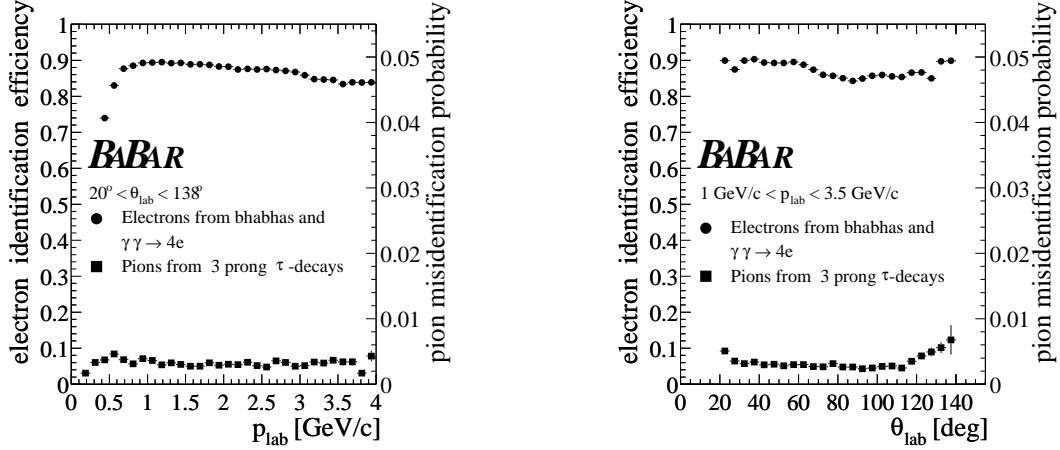


Figure 10: Electron identification efficiency and pion misidentification for the very tight selection criteria as a function of momentum (left) and polar angle (right) (note the different scales for electrons and pions).

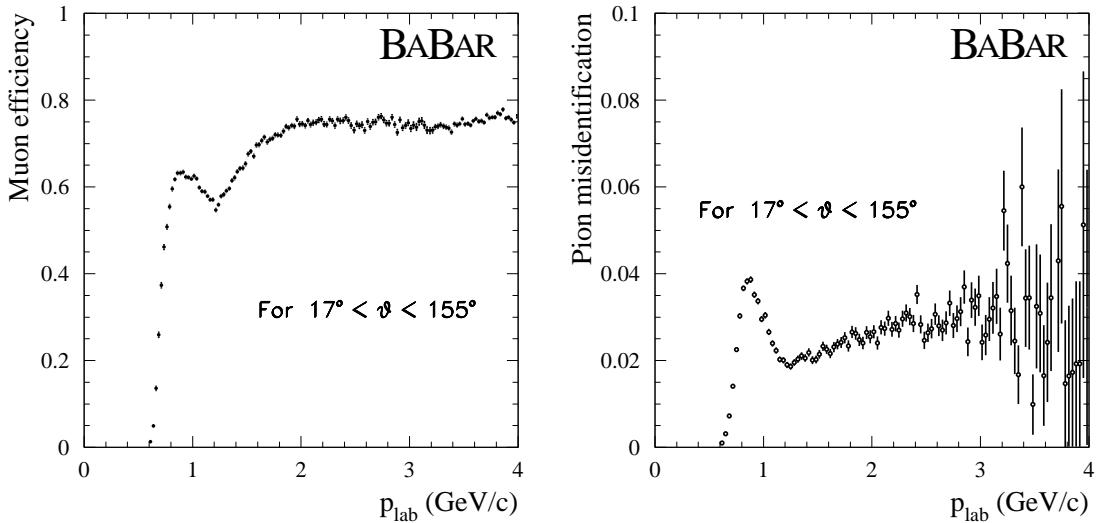


Figure 11: Muon identification efficiencies (left) and pion misidentification rates (right) for the tight muon selector, showing average efficiencies of 75% and misidentification rates of 2.5% for the momentum range 1.5 to 3 GeV/c.

$\pi^+\pi^-$ for pions. The selection of the control samples is based on kinematic variables and particle identification. No muon requirements are applied to the tracks that are used as a control sample, in order to avoid any bias in the determination of the particle identification performance. Different muon selection criteria with different levels of purity are defined for analysis specific applications. In the range $1 < p < 3 \text{ GeV}/c$ the average efficiency is about 77% for muons with a 2.5% pion fake

rate (see Figure 11).

7.1.3 Charged hadrons

Kaons are selected using the information from the SVT, DCH, and DIRC systems. Likelihoods are calculated from the dE/dx measurements in the SVT and DCH, and from the angle and number of photons found in the Cherenkov ring in the DIRC. The individual likelihoods from the three detectors are then multiplied together and a cut on the ratio of likelihoods (K vs π , K vs p) is applied:

$$L_\pi \cdot r < L_K \text{ and } L_p \cdot r < L_K \quad (4)$$

Various kaon selections have been implemented, achieving different levels of efficiency and purity. Each detector output is used only in a specific interval in momentum. For example, for a tight selection, the ranges used for each subdetector are 0.025–0.7 GeV/ c for SVT, 0.090–0.7 GeV/ c for DCH, and > 0.6 GeV/ c for the DIRC. The minimum requirements for a track to be considered in the individual subdetectors are 2 and 10 dE/dx samples for the SVT and DCH respectively, and track extrapolation within the DIRC acceptance (number of expected photons greater than zero). Finally, the value of likelihood ratio r was dependent on the momentum of the tracks to be identified. In the tight mode, the intervals and ratio requirements were:

$$\begin{array}{ll} 0.5 - 0.7 \text{ GeV}/c & r = 15 \\ 0.7 - 2.7 \text{ GeV}/c & r = 1 \\ > 2.7 \text{ GeV}/c & r = 80 \end{array}$$

The performance of the various selections has been measured with data using control samples of kaons and pions from the kinematically identified decays: $K_S^0 \rightarrow \pi^+\pi^-$ and $D^{*+} \rightarrow D^0(\rightarrow K^-\pi^+)\pi^+$. To select the K_S^0 sample, very tight cuts are used (e.g. on the angle between the K_S^0 candidate vertex direction and the vertex momentum direction, on the decay distance from the interaction point, on the reconstructed K_S^0 candidate mass). The plot of the invariant mass of the $\pi^+\pi^-$ pairs is shown in Figure 12(left); the purity of the resulting pion sample is $> 99\%$. The D^{*+} sample, obtained with a tight cut on the difference between the $K\pi\pi$ and $K\pi$ masses ($0.1445 < \Delta M < 0.1465$ MeV/ c^2) shown in Figure 12(right), has a combinatorial background of around $\sim 13\%$ (for a kaon sample purity of $\sim 90\%$, with the purity higher at higher momenta). In determining particle identification performance, a correction for the background contribution has been made in each momentum bin using sideband subtraction.

The measured kaon efficiency and pion misidentification rates are shown in Figure 13 for the tight selection based the D^{*+} sample. The efficiency is found to be 90%, while misidentification rate is 2.5%, averaged over the full momentum range. Note that these results are highly dependent on the momentum spectrum of the kaons and pions in the particular samples used in an analysis.

7.2 Neutral Particle Identification

7.2.1 Photons

Photons are detected in the EMC where adjacent crystals with energy deposits exceeding 1 MeV are grouped in clusters. Channels marked as noisy by online or offline monitoring are excluded. Clusters with more than one local energy maximum are then split into “bumps” and the energy of each crystal is partially assigned to each bump by a simultaneous iterative adjustment of the centers and energies of the bumps, assuming electromagnetic shower shapes. In the next stage all

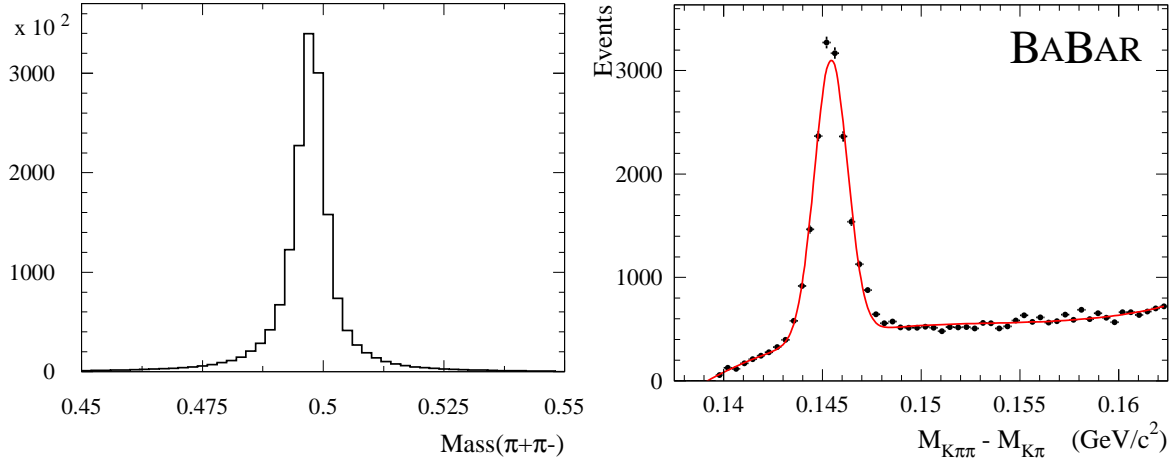


Figure 12: Mass distribution (left) of K_S^0 candidates used to select a pion control sample. Distribution (right) of the difference of the D^* and D^0 candidate masses, used to select control samples of kaons and pions.

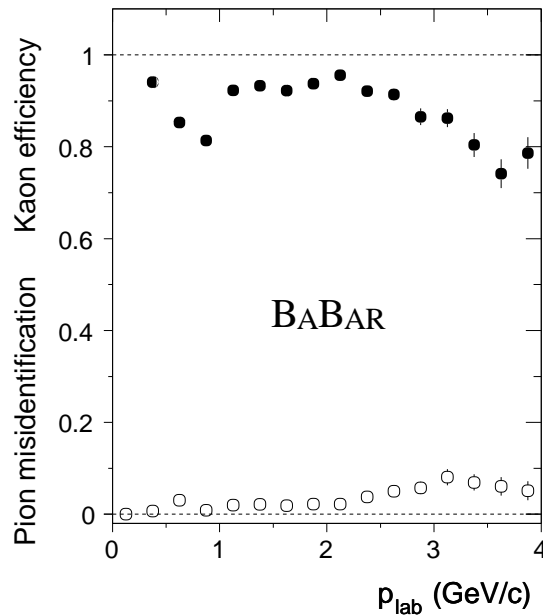


Figure 13: Kaon efficiency (filled points) and pion misidentification (open points) for a tight kaon selection, measured with a D^* decay control sample.

charged tracks reconstructed in the tracking volume are extrapolated to the EMC entrance and a track–bump matching probability is calculated for each pair. All bumps with a small matching probability are treated as photon candidates. A small number of these candidates, where the bump shape is incompatible with that expected of an electromagnetic shower, are rejected. In the majority of physics analyses, photon candidates lying anywhere within the instrumented EMC

volume are used if their energy is above 30 MeV.

7.2.2 π^0 and η Reconstruction

Neutral pion and η candidates are formed from pairs of photon candidates assumed to originate from the interaction point. The invariant mass spectrum of all such pairs is shown in Figure 14 for ($E_\gamma > 30$ MeV, $E_{\gamma\gamma} > 300$ MeV) and ($E_\gamma > 100$ MeV, $E_{\gamma\gamma} > 1$ GeV), where clear π^0 and η peaks can be seen. The π^0 mass resolution in multihadron events is 6.9 MeV/ c^2 , while in low occupancy $\tau\tau$ events it is 6.5 MeV/ c^2 for π^0 energies below about 1 GeV/ c . Improved resolution is also observed in hadronic events where only isolated photons are considered. The η mass resolution is 16 MeV/ c^2 . The π^0 and η mass peaks from inclusive multihadron events are also shown in Figure 14. The signal-to-background ratio for the η can be improved by vetoing photons participating in candidates in the π^0 signal region. Combinatorial background in hadronic events is suppressed by a factor of 5 by this veto requirement, with a signal loss of only 25%.

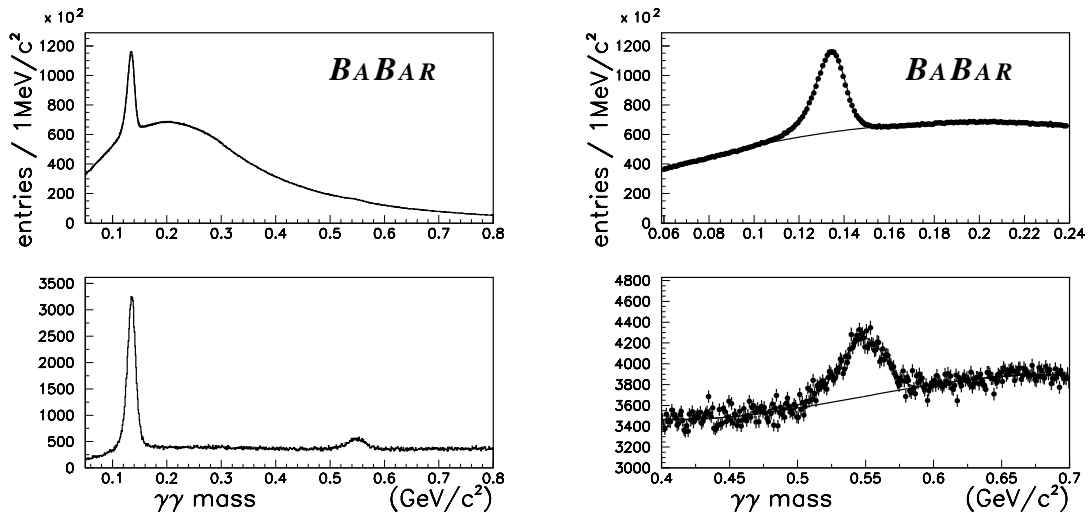


Figure 14: Invariant mass of $\gamma\gamma$ pairs from hadronic events. Upper pair of plots are for $E_\gamma > 30$ MeV and $E_{\gamma\gamma} > 300$ MeV, with enlargement of the π^0 mass region on the right; lower pair of plots are for $E_\gamma > 100$ MeV and $E_{\gamma\gamma} > 1$ GeV, with enlargement of the η mass region on the right.

The detector segmentation and achieved spatial resolution allow the reconstruction of π^0 's with photon separation in the electromagnetic calorimeter as small as 5 cm, although with some deterioration of the resolution. The small fraction of high energy π^0 whose photons cannot be resolved into individual photon bumps ($\approx 10\%$ in the 4–6 GeV region) can be separated from single photons using the cluster shape (the second moment of the energy distribution around the cluster centroid).

Large samples of inclusive and exclusive data have been used for simulation comparison studies. The π^0 mass value, resolution, and efficiency, and their (weak) energy dependence were found to be in very good agreement. Furthermore, the π^0 mass, width, and yield, are monitored in real time during data collection and reconstruction. Limits on the possible discrepancies between the data and the simulation for the photon energy scale, resolution, and reconstruction efficiency, have been

conservatively set to be 0.75%, 1.5% and 2.5% respectively.

7.2.3 Neutral Hadrons

- $K_S^0 \rightarrow \pi^+\pi^-$

To reconstruct K_S^0 candidates, we consider any pair of oppositely-charged tracks combined in a common vertex. No cut is made on the probability of χ^2 , but the vertex fit must converge. The reconstructed momentum of the K_S^0 candidate is required to be aligned with the direction between the interaction point and the reconstructed vertex. Finally, a minimum transverse momentum of the daughters with respect to the flight direction is required in order to eliminate combinatorial and Λ contamination. For Figure 15, a tighter selection is applied on a small data sample; the χ^2 probability is required to be greater than 0.01, the angle between the direction of flight and the direction from the interaction point to the reconstructed vertex is required to be greater than 45 mrad, the transverse momentum of the daughters with respect to the K_S^0 flight direction is required to be between 0.11 and 0.22 GeV/c.

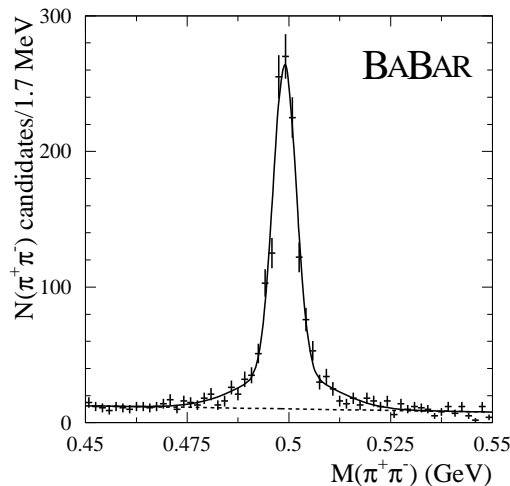


Figure 15: K_S^0 mass resolution (tight selection). The fit is performed with a double Gaussian, the central Gaussian contains 70% of the events and has a width of 2.82 ± 0.19 MeV/ c^2 .

- $K_S^0 \rightarrow \pi^0\pi^0$

Non-overlapping π^0 candidates are combined to construct $K_S^0 \rightarrow \pi^0\pi^0$ candidates. For each candidate with an energy above 800 MeV and a mass between 300 and 700 MeV/ c^2 , we determine the most probable decay vertex along the path defined by its momentum vector and the primary vertex. The point where the product of the probabilities from the two π^0 mass constraint fits is a maximum is chosen as the K_S^0 decay vertex. We demand that this point lie in a region between -10 and $+40$ cm from the primary vertex and that the K_S^0 mass at that point is in the range 470–536 MeV/ c^2 . This method [18] improves significantly the mass scale and resolution. A vertex resolution of 5 cm along the flight direction is predicted by the simulation. The inclusive K_S^0 mass peak from real data, exhibiting a resolution better than 10 MeV/ c^2 , is shown in Figure 16.

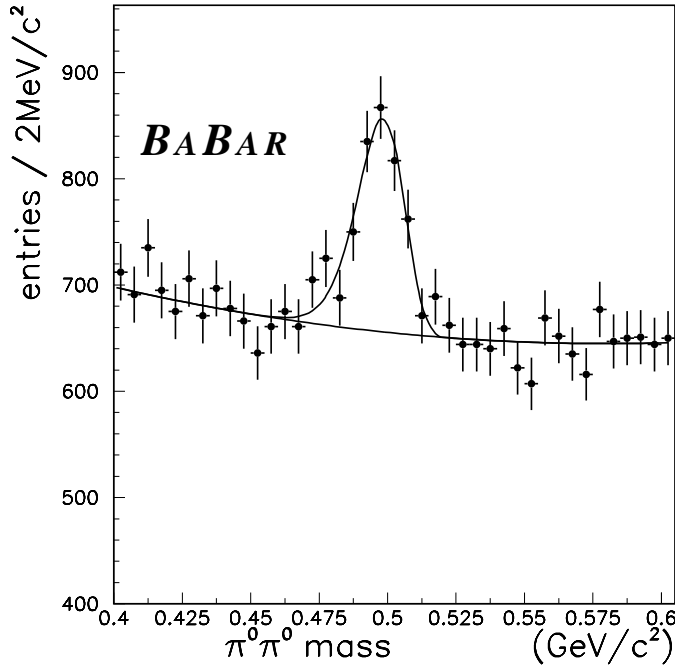


Figure 16: $\pi^0\pi^0$ mass spectrum and K_S^0 signal from hadronic events

- K_L^0

The EMC and IFR detectors are both used for the detection of K_L mesons, which are reconstructed as neutral clusters that cannot be associated with any charged track in the event. In the EMC, the background consists primarily of photons and high energy π^0 s. We are able to distinguish K_L clusters from these backgrounds by using a shower shape analysis, performed by expanding the shape into a series of Zernike moments. For clusters with an energy greater than 500 MeV, a single Zernike moment (2,0) is sufficient to discriminate K_L mesons and photons. Between 200 and 500 MeV, a two-dimensional cut ((2,0) and (4,2)) is used. Below 200 MeV, we are unable to sufficiently discriminate between photons and K_L mesons. IFR clusters are defined and selected as hits in two or more resistive plate chamber layers. The background is dominantly charged particles and detector noise. Some splitoffs from charged hadronic showers are missed by the tracking association, due to the irregular structure of these showers. We suppress these clusters by rejecting K_L candidate clusters close to any track in the event.

The performance of the K_L identification is demonstrated in Figure 17a, using events from $e^+e^- \rightarrow \gamma(\phi \rightarrow K_S K_L)$. In these events, the position and energy of the K_L can be constrained from the measured photon and K_S kinematics. Figures 17b and 17c illustrate the performance of the K_L selection. We observe good agreement between Monte Carlo simulations and the data. The efficiency for K_L reconstruction agrees to within the current statistical error, which is approximately 10% for both IFR and EMC selections.

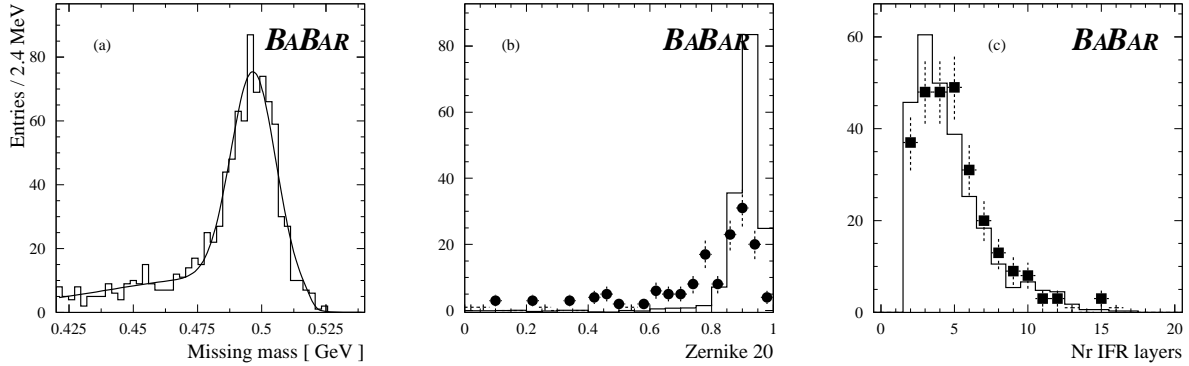


Figure 17: The missing mass distribution ($p_{K_L}^2$) of candidate $\phi\gamma$ events is shown in (a). We find $594 \pm 40 e^+e^- \rightarrow \gamma(\phi \rightarrow K_S K_L)$ events. Using these events, (b) shows the comparison of the Zernike moment (2,0) distribution for clusters from K_L mesons (points) and photons (histogram). A comparison between data (points) and Monte Carlo (histogram) is shown in (c) for the number of hit layers in the Instrumented Flux Detector (plot (c) is absolutely normalized).

8 Common Analysis Issues

8.1 Centre of Mass Energy and Boost

The beam energies provided by PEP-II are obtained with an algorithm capable of tracking variations to within about 1 MeV, and are used to determine the time-dependence of the centre of mass energy. The absolute energy scale is determined from a sample of fully-reconstructed B candidates (a recent measurement of the B mass by CLEO [13] is used).

We define two main coordinate systems:

- A *BABAR* coordinate system (LAB), linked to the *BABAR* detector. The z axis is along the DCH axial wires, the y axis is vertical (upward) and the x axis points towards the exterior of the PEP-II rings. The *BABAR* z axis and the PEP-II electron beam are not exactly aligned. The former is tilted in the horizontal plane by 19 mrad with respect to the beam axis.
- A centre-of-mass coordinate system (CMS), a frame where the two beams have equal energy $E_b^* = \sqrt{s}/2$ (where E_b^* is the centre-of-mass beam energy). The z axis of the CMS lies along the electron beam direction (this is the relevant choice for most physics quantities). The Lorentz transformation from LAB into CMS quantities is the product of a rotation that aligns the z' axis of the rotated frame with the boost direction, and a Lorentz boost along the new z' into the CMS frame. The rotation angles are determined on a run-by-run basis from the opening angle and flight direction of $\mu^+\mu^-$ and e^+e^- events, and are verified against the orientation of the collision spot for the beams. The magnitude of the boost is obtained from the PEP-II energies.

8.2 Continuum Rejection Variables

We use common shape variables, computed with charged tracks in the centre of mass frame, to preferentially reject continuum events. The most important of these variables are thrust, sphericity and $R2$, the ratio of 2nd to 0th Fox-Wolfram moments.

- **Thrust:** The thrust axis, \hat{T} , of an event is defined to be the direction that maximizes the sum of the longitudinal momenta of the particles. The value of the thrust T must lie in the range 0.5 to 1, where $T \sim 1$ corresponds to a highly directional event and $T \sim 0.5$ to an isotropic event.
- **Sphericity:** Sphericity is a measure of the sum of squares of transverse momenta for each track with respect to the event axis. Highly directional events have low sphericity whereas isotropic events tend to have sphericities close to one.
- **Fox-Wolfram moments:** The ℓ^{th} Fox-Wolfram moment is momentum-weighted sum of Legendre polynomial of the ℓ^{th} order computed from the cosine of the angle between all pairs of tracks. The ratio $R2$ of Fox-Wolfram 2nd to 0th moments is the variable which provides the best separation between $B\bar{B}$ signal and continuum. Jet-like continuum events tend to have higher values of $R2$ than the more spherical $B\bar{B}$ events.

8.3 Event Selection and B Counting

8.3.1 Fiducial regions

The acceptance region in polar angle for charged tracks, corresponding to full SVT coverage, ranges from a minimum of 410mr with respect to the z axis in the forward direction to 602mr in the backward direction ($0.41 < \theta < 2.54$). For neutral clusters, the fiducial region is reduced to an angle 732mr with respect to the z axis in the backward direction ($0.41 < \theta < 2.41$) to account for the more limited EMC coverage in the backward region.

8.3.2 Multi-Hadron selection

Multi-hadron event selection is designed to have a very high efficiency for $B\bar{B}$ events while keeping the systematic uncertainties on the determination of that efficiency as low as possible. The contribution of continuum and τ pair events in the sample is reduced by a cut on $R2$. Using only tracks and clusters in fiducial volume described above, the selection criteria are as follows:

- Four or more charged tracks, at least three of which must have associated DCH information
- Primary vertex within 5 mm in x and y of the nominal beam spot position,
- $R2$ less than 0.7,
- Total energy greater than 5 GeV.

The efficiency for $B\bar{B}$ events is 96%, while the contamination due to beam gas, two-photon and tau pair events is approximately 2%.

8.3.3 Muon pair selection

In the centre of mass frame, events containing two charged tracks with momenta larger than 2 GeV/ c and 4 GeV/ c , respectively, and with angle with respect to the beam axis greater than 725mr are selected. The two tracks must have an acolinearity smaller than 10° . The mass of the pair must be larger than 7.5 GeV/ c^2 . The total energy deposited in the calorimeter by the two particles must be smaller than 1 GeV. The event is rejected if neither track has an associated energy measurement.

8.4 Offline Luminosity Determination

The integrated luminosity recorded by *BABAR* is determined offline using Bhabha, muon pair, and gamma-gamma events. The measurement precision is limited by systematic errors in all cases to the several percent level, although this clearly can be improved to 0.5% or better. The systematic uncertainty for the Bhabha measurement is dominated by the efficiency corrections for the Bhabha veto by the Level 3 trigger, and by theoretical uncertainties on the differential Bhabha cross section. Likewise, we are still in the process of comparing and understanding Monte Carlo generators for muon pair events, including proper treatment of radiative events. A better understanding of the impact of occasional hot towers in the EMC will improve the systematic error on the gamma-gamma luminosity. The luminosity determinations are consistent at the several percent level, but are much better than this for tracking relative luminosity and the variation with beam conditions.

8.5 B Counting

We estimate the number of $B\bar{B}$ pairs $N_{B\bar{B}}$ from the total number of events passing the hadronic event selection N_{MH} and the total number of events passing the muon pair selection $N_{\mu\mu}$:

$$N_{B\bar{B}} = N_{MH}^{\text{on}} - \kappa \times N_{MH}^{\text{off}} \times \frac{N_{\mu\mu}^{\text{on}}}{N_{\mu\mu}^{\text{off}}} \quad , \quad (5)$$

where the superscript *on* refers to on-resonance data and *off* to off-resonance. κ is a factor close to 1 that corrects for changes in efficiency and cross section with center of mass energy. It is estimated by Monte Carlo to be 0.9962. The systematic error on $N_{B\bar{B}}$ is 1.7%, dominated by the variation between running periods of the ratio $N_{MH}^{\text{off}}/N_{\mu\mu}^{\text{off}}$.

Branching fraction measurements frequently use the number of *produced* $B\bar{B}$ pairs. The efficiency for $B\bar{B}$ events to pass the selection criteria is determined by Monte Carlo to be 96.0%. The total systematic error on the number of produced $B\bar{B}$ pairs is 3.6%.

8.6 Exclusive B Reconstruction Variables

8.6.1 Kinematic variables

A number of kinematic quantities could be used to characterize the reaction $e^+e^- \rightarrow B\bar{B}$ where one of the B mesons is fully reconstructed. However, our goal is to select a pair of such kinematic variables, having little correlation between them, that make use of the maximum available information for optimal background rejection.

At the $\Upsilon(4S)$ resonance the B mesons are produced with very small Q values. As a result their center-of-mass energy E^* and momentum p^* are very sensitive to fluctuations of the center-of-mass beam energy $E_b^* = \sqrt{s}/2$. In contrast, the variable ΔE defined as:

$$\Delta E = E^* - E_b^* \quad , \quad (6)$$

is relatively insensitive to E_b^* fluctuations.

The distribution of ΔE is peaked at zero for $e^+e^- \rightarrow B\bar{B}$ events, and its width is governed in most cases by the beam energy measurement error σ_E^2 . It is not necessary to boost the B candidate to the center-of-mass frame to compute ΔE , as can be seen by writing ΔE in an explicitly Lorentz invariant form:

$$\Delta E = \frac{2\tilde{P} \cdot \tilde{P}_i - s}{2\sqrt{s}} \quad , \quad (7)$$

where \tilde{P} and \tilde{P}_i are the Lorentz vectors representing the B candidate four momentum and the initial-state four momentum respectively.

The ΔE variable is used in conjunction with either one of the following two mass variables:

- **Beam-energy substituted mass** m_{ES} , defined as:

$$m_{\text{ES}} = \sqrt{\left(\frac{\frac{1}{2}s + \vec{p} \cdot \vec{p}_i}{E_i}\right)^2 - p^2} \quad , \quad (8)$$

where E_i and \vec{p}_i are the total energy and the three momentum of the initial state in the laboratory frame, and \vec{p} is the three momentum of the B candidate in the same frame. At a symmetric machine (where $\vec{p}_i = \vec{0}$) this variable is obtained simply by substituting the beam energy E_b^* from the measured B candidate energy E^* :

$$m_{\text{ES}} = \sqrt{E_b^{*2} - p^{*2}} \quad . \quad (9)$$

This is the definition of the variable used in ARGUS and CLEO publications under the name ‘‘beam-constrained’’ mass. The advantage of using definition of Eq. 8 at an asymmetric machine, where one needs to assign masses to candidates in order to boost to the center of mass frame, is that m_{ES} is computed in the laboratory frame without any prior commitment to the identification of particles among the B daughters.

- **Beam-energy constrained mass** m_{EC} , defined as:

$$m_{\text{EC}} = \sqrt{\hat{E}^2 - \hat{p}^2} \quad , \quad (10)$$

where \hat{E} and \hat{p} are center-of-mass frame quantities obtained by performing a kinematic fit with the $E^* = E_b^*$ constraint.

The two choices $(\Delta E, m_{\text{ES}})$ and $(\Delta E, m_{\text{EC}})$ are almost equivalent. For certain analyses, it may be helpful to exploit the property that m_{ES} does not require daughter mass assignments, while the kinematical fit performed for m_{EC} makes optimal use of the information collected by the detector. In addition, the pair $(\Delta E, m_{\text{EC}})$ has the smallest correlation.

8.6.2 Background parametrisation

To describe the background shape in beam-energy constrained mass plots, we use the ARGUS distribution [14] given by:

$$\mathcal{A}(m | m_0, c) = \frac{\theta(m < m_0)}{N} \times m \sqrt{1 - (m/m_0)^2} \times \exp \left[c(1 - m/m_0)^2 \right] \quad , \quad (11)$$

where m_0 represents the kinematic upper limit and is generally held fixed at the center-of-mass beam energy E_b^* .

9 Conclusions and Prospects

Since the start of running at PEP-II in May 1999, the *BABAR* experiment has accumulated over 12.7 fb^{-1} of data. Many of the detector sub-systems have reached their design goals and significant progress has been made towards understanding the performance of the detector. Several preliminary measurements with the *BABAR* detector are to be presented at this conference. We anticipate having a data set equivalent to a significantly larger integrated luminosity by the end of this year. Thus, the results presented here are just the beginning of an exciting program of physics with *BABAR* at PEP-II. In future years, we expect to be able to undertake detailed studies of *CP* violation in the *B* meson system.

10 Acknowledgments

We are grateful for the contributions of our PEP-II colleagues in achieving the excellent luminosity and machine conditions that have made this work possible. We acknowledge support from the Natural Sciences and Engineering Research Council (Canada), Institute of High Energy Physics (China), Commissariat à l'Énergie Atomique and Institut National de Physique Nucléaire et de Physique des Particules (France), Bundesministerium für Bildung und Forschung (Germany), Istituto Nazionale di Fisica Nucleare (Italy), The Research Council of Norway, Ministry of Science and Technology of the Russian Federation, Particle Physics and Astronomy Research Council (United Kingdom), the Department of Energy (US), and the National Science Foundation (US). In addition, individual support has been received from the Swiss National Foundation, the A. P. Sloan Foundation, the Research Corporation, and the Alexander von Humboldt Foundation. The visiting groups wish to thank SLAC for the support and kind hospitality extended to them.

References

- [1] An Asymmetric *B* Factory Based on PEP, The Conceptual Design Report for PEP-II LBNL Pub 5303, SLAC-372 (1991).
- [2] Status Report on PEP-II Performance, J. Seeman *et al.*, to appear in the Proceedings of the VIIth European Part. Acc. Conf. - EPAC 2000, Vienna, Austria, (June 2000).
- [3] *BABAR* Technical Design Report, *BABAR* Collaboration, SLAC-REP-372 (1995).
- [4] The *BABAR* Silicon Vertex Tracker, C. Bozzi *et al.*, Nucl. Instr. and Methods **A435** (1999) 25.
- [5] R. Santonico and R. Cardarelli, Nucl. Instr. and Methods **A187** (1981) 377.
- [6] A. Ryd *et al.* EvtGen User Guide:
<http://www.slac.stanford.edu/BFROOT/doc/LIGHT/6.7.5/src/EvtGen/guide/>
- [7] "GEANT, Detector Description and Simulation Tool", CERN Program Library Long Writeup W5013, (1994).
- [8] H. C. Fesefeldt, Technical Report PITHA 85-02, III, Physikalisches Institut, RWTH Aachen Physikzentrum, 5100 Aachen, Germany, (1985).

- [9] P. A. Aarnio *et al.*, FLUKA86 User's Guide, CERN Technical Report TIS-RP-168, (1986); P. A. Aarnio *et al.*, Enhancements to the FLUKA86 Program (FLUKA87), CERN Technical Report TIS-RP-190, (1987).
- [10] C. Zeitnitz and T. A. Gabriel, "The Geant-Calor Interface User's Guide": http://dipmza.physik.uni-mainz.de/~www_aleph/zeitnitz.c/gcalor_manual.ps, (1996).
- [11] David N. Brown, Eric A. Charles, and Douglas A. Roberts, The *BABAR* Track Fitting Algorithm, Proceedings of CHEP 2000, (M. Mazzucato, ed.), Padova, Italy (Feb. 2000).
- [12] The *BABAR* Physics Book, P.F. Harrison and H.R. Quinn editors, SLAC-REP-504 (1998).
- [13] S.E. Csorna *et al.* (CLEO Collaboration), Phys. Rev. **D61** (2000) 111101.
- [14] H. Albrecht *et al.* (ARGUS Collaboration), Phys. Lett. **B185** (1987) 218.
- [15] Statistical and Computational Methods in Data Analysis, Siegmund Brandt, North Holland Publishing.
- [16] A. Drescher *et al.*, Nucl. Instr. and Methods **A237** (1985) 464.
- [17] R. Sinkus and T. Voss, Nucl. Instr. and Methods **A391** (1990) 360.
- [18] R. Adler *et al.* (CPLEAR Collaboration), Z. Phys. **C70** (1996) 211.